

Combined Scaling for Zero-shot Transfer Learning

Hieu Pham*

Zihang Dai*

Golnaz Ghiasi*

Kenji Kawaguchi*

Hanxiao Liu

Adams Wei Yu

Jiahui Yu

Yi-Ting Chen

Minh-Thang Luong

Yonghui Wu

Mingxing Tan

Quoc V. Le

*: *Equal contributions.*

Corresponding authors: {HYHIEU,ZIHANGD}@GOOGLE.COM.

HYHIEU@GOOGLE.COM

ZIHANGD@GOOGLE.COM

GOLNAZG@GOOGLE.COM

KAWAGUCH@CSAIL.MIT.EDU

HANXIAOL@GOOGLE.COM

ADAMSYUWEI@GOOGLE.COM

JIAHUIYU@GOOGLE.COM

YITINGCHEN@GOOGLE.COM

THANGLUONG@GOOGLE.COM

YONGHUI@GOOGLE.COM

TANMINGXING@GOOGLE.COM

QVL@GOOGLE.COM

Editor: *To be assigned.*

Abstract

We present a combined scaling method – named BASIC – that achieves 85.7% top-1 accuracy on the ImageNet ILSVRC-2012 validation set without learning from any labeled ImageNet example. This accuracy surpasses best-published similar models – CLIP and ALIGN – by 9.3%. Our BASIC model also shows significant improvements in robustness benchmarks. For instance, on 5 test sets with natural distribution shifts such as ImageNet-{A,R,V2,Sketch} and ObjectNet, our model achieves 84.3% top-1 average accuracy, only a small drop from its original ImageNet accuracy.

To achieve these results, we scale up the contrastive learning framework of CLIP and ALIGN in three dimensions: data size, model size, and batch size. Our dataset has 6.6B noisy image-text pairs, which is 4x larger than ALIGN, and 16x larger than CLIP. Our largest model has 3B weights, which is 3.75x larger in parameters and 8x larger in FLOPs than ALIGN and CLIP. Finally, our batch size is 65536 which is 2x more than CLIP and 4x more than ALIGN.

We encountered two main challenges with the scaling rules of BASIC. First, the main challenge with implementing the combined scaling rules of BASIC is the limited memory of accelerators, such as GPUs and TPUs. To overcome the memory limit, we propose two simple methods which make use of gradient checkpointing and model parallelism. Second, while increasing the dataset size and the model size has been the defacto method to improve the performance of deep learning models like BASIC, the effect of a large contrastive batch size on such contrastive-trained image-text models is not well-understood. To shed light on the benefits of large contrastive batch sizes, we develop a theoretical framework which shows that larger contrastive batch sizes lead to smaller generalization gaps for image-text models such as BASIC.

Contents

1	Introduction	4
2	Related Work	5
3	Background on Image-text Contrastive Learning and Zero-shot Transfer Learning	7
4	Batch Size Scaling with Pipelining and Gradient Accumulation	7
4.1	The Memory Bottleneck for Image-Text Contrastive Learning	7
4.2	Modifying Pipelining and GradAccum for the Contrastive Loss	8
5	Batch Size Scaling with the Single-Program Multiple-Data (SPMD) Scheme	10
5.1	Weight Sharding	11
5.2	Rematerialization	12
5.3	Comparison with Pipelining and Gradient Accumulation	13
6	Theoretical Insight on the Role of Contrastive Batch Size	14
7	Data and Model Scaling	17
7.1	Larger image-text dataset	17
7.2	Larger Model Architectures	17
8	Pretraining and Finetuning	17
9	Experiments	18
9.1	Training details	18
9.2	Results on Image Classification Benchmarks	19
9.3	Results on Robustness Benchmarks	19
10	Ablation Study	21
10.1	The Importance of Batch Size Scaling	21
10.2	Data Scaling, Model Scaling, and Pretraining	22
11	Limitations	23
12	Conclusion	23
A	Model sizes	29
B	Hyperparameters and other implementation details	29
C	Evaluation Datasets Details	30
D	Further Discussion on Robustness	30
E	Computational Cost	31
F	Qualitative Analysis: Successful Classification Examples	31

G	Failure Analysis	32
G.1	The benchmarks where BASIC fails	32
G.2	Example failure cases	33
H	Proofs	36
H.1	General case	36
H.1.1	Analyzing $\sup_{x \in \mathcal{X}} \mathcal{R}_B(\mathcal{H}_{\mathcal{F}, \mathcal{G}, e}^x)$ and $\mathcal{R}_m(\mathcal{H}_{\mathcal{F}, \mathcal{G}, \hat{\ell}_B})$	40
H.1.2	Combining all together for the general case	43
H.2	Bounding $\mathbb{E}_{y, \sigma} \left[\sup_{G \in \mathcal{G}} \frac{1}{B} \left\ \sum_{i=1}^B \sigma_i G(y_i) \right\ _2 \right]$ and $\sum_{k=1}^D (\mathcal{R}_m(\mathcal{F}_k) + \mathcal{R}_m(\mathcal{G}_k))$ for the special case with deep neural networks	44
H.3	Combining all together for the special case with deep neural networks	46

1. Introduction

The recent advances in multimodal training approaches such as CLIP (Radford et al., 2021) and ALIGN (Jia et al., 2021) have the potential to eliminate the need for collecting labeled training data for every new application. Using natural language as a weak supervision signal, CLIP and ALIGN achieve the impressive top-1 accuracy of 76.2% and 76.4% on ImageNet ILSVRC-2012 without learning from any labeled ImageNet data. In addition to the promising accuracy on ImageNet, the so-called “zero-shot” models in CLIP and ALIGN demonstrate two important properties. First, these models are versatile, as they can be directly deployed on many downstream tasks without task-specific data for finetuning. Second, CLIP and ALIGN models are more robust than traditional classifiers. Robustness evaluations on benchmarks with natural distribution shifts (Hendrycks et al., 2021b,a; Recht et al., 2019; Barbu et al., 2019; Wang et al., 2019) show that the accuracy of models like CLIP and ALIGN typically drops less than 10%, while the accuracy of supervised and semi-supervised models might drop as much as 40% (Taori et al., 2020; Szegedy et al., 2013).

Despite their versatility and robustness, the best models from CLIP and ALIGN are still not as competitive as supervised and semi-supervised models when enough labeled data is available, which can limit their potential applications. For example, the best CLIP and ALIGN models have an accuracy around 76% on ImageNet, which is only comparable with a supervised ResNet-50 (He et al., 2015), and significantly worse than the state-of-the-art supervised training on ImageNet (without extra data: 87.1% (Yuan et al., 2021), and with extra data: 90.88% (Dai et al., 2021)). Therefore, narrowing the gap from these models to supervised and semi-supervised models would make the image-text contrastive learning approach in CLIP and ALIGN a viable alternative for image classification.

In this paper, we develop significantly better image classifiers that leverage the image-text contrastive learning approaches like CLIP and ALIGN at a much larger scale. In particular, we scale up the contrastive learning framework of CLIP (Radford et al., 2021) and ALIGN (Jia et al., 2021) in 3 dimensions: dataset size, model size, and batch size. For the data, we expand the ALIGN dataset (Jia et al., 2021) from 1.7B noisy image-text pairs to 6.6B pairs, *i.e.*, almost 4x larger. For the models, we choose CoAtNet, an architecture with higher learning capacity (Dai et al., 2021), and scale it to 3B parameters, *i.e.*, 3.75x more weights and 8x more FLOPs than the largest models in CLIP and ALIGN. For the batch size, we use 65536 contrastive learning examples per minibatch, *i.e.*, 2x more than CLIP and 4x more than ALIGN.

Overview of our implementation. The fundamental bottleneck of training large models at larger batch sizes is the limited memory of deep learning accelerators such as GPUs and TPUs. We propose two approaches that allow practitioners to overcome such memory limits.

Our first approach (Section 4) makes use of micro-batch pipelining (Huang et al., 2019) and gradient accumulation (GradAccum) (Ott et al., 2018; Zhai et al., 2021). Our second approach (Section 5) utilizes the model parallelism scheme of Single-Program Multi-Data (SPMD) (Lepikhin et al., 2020; Xu et al., 2021) to distribute the weights of certain layers in our networks onto different devices. While our SPMD approach is faster than our pipelining approach, and can deliver exact computations, the SPMD approach requires more manual designs to scale to arbitrarily large contrastive batch sizes, and hence, is less general than the pipelining approach.

Both our pipelining approach and our SPMD approach make use of *gradient checkpointing* (Chen et al., 2016), which is also called *rematerialization* in certain literature (Kumar et al., 2019; Jain et al., 2020). The idea behind rematerialization is to discard certain intermediate values in the forward pass of a neural network to save memory, and then recompute – *i.e.*, rematerialize – these values only when they are needed for gradient computation in the network’s backward pass.

Overview of our theoretical insights. While the benefits of large datasets and large models for deep learning models have become established knowledge, the benefits of large batch size are less well-understood in the context of relatively new image-text contrastive models. To understand such benefits, we develop a theoretical analysis of the image-text contrastive learning framework of CLIP and ALIGN. Our analysis establishes that using a larger contrastive batch size in CLIP and ALIGN’s framework leads to a smaller generalization gap of the resulting models.

	ALIGN (Jia et al., 2021)	CLIP (Radford et al., 2021)	BASIC (ours)
ImageNet	76.4	76.2	85.7 (+9.3)
ImageNet-A	75.8	77.2	85.6 (+8.4)
ImageNet-R	92.2	88.9	95.7 (+3.5)
ImageNet-V2	70.1	70.1	80.6 (+10.5)
ImageNet-Sketch	64.8	60.2	76.1 (+11.3)
ObjectNet	72.2	72.3	82.3 (+10.1)
Average	74.5	74.2	84.3 (+10.1)

Table 1: Highlights of our key results. Shown are the top-1 accuracy of our method, BASIC, and similar baselines – CLIP and ALIGN – on ImageNet and other robustness test sets. None of these models have learned from any labeled training example in ImageNet. On average, BASIC surpasses the baselines by the significant **10.1** percentage points.

Overview of our empirical results. Our proposed method, called **BASIC**, for **B**atch, **D**ata and **M**odel **S**Ize **C**ombined **S**caling, achieves drastic improvements over CLIP and ALIGN models. For instance, on ImageNet, the largest BASIC model achieves 85.7% top-1 accuracy, without learning from any labeled example in the ImageNet training set. This result surpasses similar models in CLIP and ALIGN 9.3%. This BASIC model also shows significant improvements on robustness benchmarks. For instance, on 5 test sets with natural distribution shifts such as ImageNet-{A,R,V2,Sketch} and ObjectNet, the model achieves an average of 83.7% top-1 accuracy, only a small drop from its original ImageNet accuracy (see Table 1). When tested against CLIP on the other 17 image classification benchmarks, *e.g.*, CIFAR, Caltech101, Flowers, etc. BASIC outperforms CLIP on 13 out of these 17 benchmarks.

2. Related Work

Large-scale pretraining and the contrastive loss. As computer vision models grow in their size and capacity, many weakly-supervised and self-supervised pretraining methods have been proposed to learn good visual representations. On one hand, pretraining with a classification loss on large weakly-labeled datasets such as Instagram hashtags or JFT can produce significant gains on downstream tasks such as ImageNet (Joulin et al., 2016; Mahajan et al., 2018; Kolesnikov et al., 2020; Dosovitskiy et al., 2021; Sun et al., 2017; Zhai et al., 2021). On the other hand, self-supervised methods which leverage existing structures in unlabeled data to train models have been developed. A promising development in self-supervised learning is the contrastive loss, with representative works like CPC (van den Oord et al., 2018), SimCLR (Chen et al., 2020a,b) and MoCo (He et al., 2020; Chen et al., 2020c). In this paper, we scale up the contrastive learning framework, which we will revisit in detail in Section 3.

Contrastive-learned image-text models. Unlike the single-modal contrastive approaches mentioned in the previous paragraph, our work leverages data from two modalities: image and text. Using images with accompanying text is related to the literature on image-captioning models, such as (Vinyals et al., 2015; Karpathy and Fei-Fei, 2015; Xu et al., 2015; Joulin et al., 2016; Li et al., 2017; Sariyildiz et al., 2020; Zhang

et al., 2020; Desai and Johnson, 2021). While learning to generate captions from images can induce good visual representations, it is not the goal of this paper. Instead, this paper focuses on establishing the ability of models to *classify images based on textual descriptions*. This focus makes our work closely related to the recent work of image-text models such as CLIP (Radford et al., 2021) and ALIGN (Jia et al., 2021). Similar to CLIP and ALIGN, our work also learns the mapping between images and texts, which is related to many previous works, such as (Hironobu et al., 1999; Weston et al., 2010; Socher and Fei-Fei, 2010; Socher et al., 2013; Hodosh et al., 2013; Frome et al., 2013; Norouzi et al., 2013; Kiros et al., 2014; Socher et al., 2014; Akata et al., 2015b,a; Nam et al., 2017; Faghri et al., 2017; Li et al., 2019; Liu et al., 2019; Lu et al., 2019; Messina et al., 2020; Chen et al., 2020d; Huang et al., 2020; Chen et al., 2021).

Differences between our work and zero-shot learning. Early works on zero-shot vision models date back to the 2000s, e.g., (Larochelle et al., 2008; Zhang et al., 2017; Xian et al., 2016, 2017; Schönfeld et al., 2019). In these works, the term “zero-shot” refers to the ability of models to “*generalize to classes or tasks for which no training data are available and only a description of the classes or tasks are provided*”. Under such definition, BASIC models – as well as the recent work that BASIC is based on such as CLIP (Radford et al., 2021) and ALIGN (Jia et al., 2021) – are *not* “zero-shot learned” models. This is because the data curating procedures of BASIC, CLIP, and ALIGN can expose certain class names to their models, albeit not intentionally. For instance, when an image of a golden retriever dog is crawled from the internet, the image could come from a file named `my_golden_retriever.jpg` which was uploaded by a user. If a model in BASIC, CLIP, or ALIGN learns to associate the content of such an image with the text sequence “my golden retriever” as parsed from the image’s file name, and then the model uses the knowledge from such association at test time, then the model is not zero-shot. Despite being *not* zero-shot, models from BASIC, CLIP, and ALIGN retain their claimed benefits on versatility and robustness.

Zero-shot transfer learning Instead of zero-shot learning, CLIP and ALIGN are known to conduct zero-shot *transfer* learning (Radford et al., 2021; Jia et al., 2021; Zhai et al., 2022). Zero-shot transfer learning differs significantly from zero-shot learning. Unlike zero-shot learning, it permits relevant supervised information during pretraining, while it allows no supervised examples during the transfer protocol; i.e., zero-shot transfer learning skips the finetuning stage completely and performs the downstream task based only on a text description of the target classes. For example, see (Radford et al., 2021; Jia et al., 2021; Zhai et al., 2022) for more details on this terminology.

Data, model and batch scaling. Scaling has proven to be a powerful tool to boost the efficacy of vision model pretraining. There are three dimensions one can scale on. The simplest dimension is data. Indeed, recent efforts have shown that the more data we train on, the better the models become (Joulin et al., 2016; Mahajan et al., 2018; Kolesnikov et al., 2020; Dosovitskiy et al., 2021; Sun et al., 2017). The second dimension is the model size, with representative works such as EfficientNet, ViTs and related works (Tan and Le, 2019, 2021; Tan et al., 2020; Dosovitskiy et al., 2021; Zhai et al., 2021; Bello et al., 2021). Lastly, scaling up batch sizes is also the key for improving the model effectiveness (Goyal et al., 2017), especially for the contrastive loss (Chen et al., 2020a; Tian et al., 2020; Jia et al., 2021; Radford et al., 2021). Our work is inspired by the power of scaling, and pushes the limits in all the dimensions.

3. Background on Image-text Contrastive Learning and Zero-shot Transfer Learning

In this section, we revisit the contrastive training framework for parallel image-text data, as introduced by CLIP (Radford et al., 2021) and ALIGN (Jia et al., 2021). In doing so, we define the notations that will be used throughout the remaining of this paper.

Let $\mathbf{x} \in \mathcal{X}$ be an arbitrary image and $\mathbf{y} \in \mathcal{Y}$ be an arbitrary text sequence. The image-text contrastive training framework (Radford et al., 2021; Jia et al., 2021) trains an image encoder F and a text encoder G to map \mathbf{x} and \mathbf{y} into a D -dimensional unit sphere, *i.e.*, $F(\mathbf{x}), G(\mathbf{y}) \in \mathbb{S}^D$. The desiderata of these encoders is that images and text sequences of similar semantics should be mapped to nearby points in the latent space, while those with different semantics should be mapped to distant points in the space. To train F and G to achieve such desiderata, a minibatch gradient training procedure is used. At each step in this training procedure, F and G receives B image-text pairs, *i.e.* $(\mathbf{x}_i, \mathbf{y}_i)$ for $i = 1, 2, \dots, B$. Based on the embeddings computed by F and G , a similarity matrix \mathbf{A} is computed, where $\mathbf{A}_{i,j} = (F(\mathbf{x}_i)^\top G(\mathbf{y}_i))/\tau$. Here, τ is called the softmax temperature which serves to steepen or dampen the softmax distributions in the rows and columns of \mathbf{A} . From this similarity matrix \mathbf{A} , two softmax-like losses are computed based on the rows and the columns of \mathbf{A} :

$$\text{RowLoss}_B = -\frac{1}{B} \sum_{i=1}^B \log \frac{\mathbf{A}_{i,j}}{\sum_{k=1}^B \mathbf{A}_{i,k}} \quad (1)$$

$$\text{ColumnLoss}_B = -\frac{1}{B} \sum_{j=1}^B \log \frac{\mathbf{A}_{i,j}}{\sum_{k=1}^B \mathbf{A}_{k,j}} \quad (2)$$

$$\text{ContrastiveLoss}_B = \frac{\text{RowLoss}_B + \text{ColumnLoss}_B}{2} \quad (3)$$

Minimizing ContrastiveLoss_B encourages the entries on the diagonal of \mathbf{A} to be large while the entries elsewhere to be small. Equivalently, images and text sequences from the same pair in the minibatch, *i.e.* x_i and y_i , will be embedded into nearby points, while those from different pairs, *i.e.* x_i and $y_{j \neq i}$, will be embedded into distant points. The resulting encoders F and G thus achieve the desiderata of the contrastive learning framework.

4. Batch Size Scaling with Pipelining and Gradient Accumulation

We start this section by discussing the memory bottleneck in the contrastive training framework as described in Section 3. We focus on memory because it is the most crucial bottleneck which hinders two out of three dimensions that we want to scale, *i.e.*, model size and batch size. We further show that the vanilla pipelining algorithm (Huang et al., 2019) with gradient accumulation (GradAccum) (Ott et al., 2018; Zhai et al., 2021) is not directly applicable to contrastive learning. We then describe our modifications to make GradAccum work for contrastive learning.

4.1 The Memory Bottleneck for Image-Text Contrastive Learning

The memory bottleneck. The consensus among representative work in contrastive learning (Chen et al., 2020b,c; He et al., 2020; Chen et al., 2020a) is that the larger the networks trained with a larger contrastive batch size performs better. This observation is further explained by our theoretical analysis in Section 6, and is confirmed by empirical results in Section 10. Therefore, we want to enlarge the networks F , G , and the batch size B . However, this will create a memory bottleneck. Three well-known techniques to relieve memory

burden are gradient accumulation (GradAccum) (Ott et al., 2018; Zhai et al., 2021), re-materialization (or gradient checkpointing) (Griewank and Walther, 2000; Chen et al., 2016) and model parallelism (Shazeer et al., 2018; Huang et al., 2019; Lepikhin et al., 2020). Note that all three techniques are orthogonal and complementary to each other. Next in section 4.2, we present an approach based on pipelining model parallelism and gradient accumulation.

Vanilla GradAccum. Consider training a model weight vector θ to minimize a loss function \mathcal{L} . For a batch of B examples $\{\mathbf{e}_1, \mathbf{e}_2, \dots, \mathbf{e}_B\}$, let g_i be the gradient of \mathcal{L} with respect to θ computed on example \mathbf{e}_i , *i.e.*, $g_i = \nabla_{\theta} \mathcal{L}(\theta; \mathbf{e}_i)$. In the standard minibatch setting, we update θ with the average batch gradient $\bar{g} = (\sum_{i=1}^B g_i) / B$. When our accelerator memory can only hold $M \ll B$ examples, GradAccum splits the batch of B examples into smaller batches with at most M examples, called *microbatches*, then computes the gradients of the microbatches, and averages them.

We now analyze the steps of GradAccum. For simplicity, assume that M evenly divides B , and that microbatch i -th consists of examples \mathbf{e}_j 's with $(i-1)M + 1 \leq j \leq iM$. With this assumption, the GradAccum procedure first initializes a zero vector \bar{g} of the same size with θ . Then, sequentially for each microbatch i -th, the microbatch gradient $c_i = (\sum_{j=(i-1)M+1}^{iM} g_j) / M$ is added to \bar{g} . In the end, \bar{g} holds the correct minibatch gradient, up to a normalization constant $K = B/M$.

GradAccum cannot be naively applied to contrastive learning. There are two properties that make GradAccum not applicable to contrastive learning. First, in order to evaluate the loss ContrastiveLoss_B in Equation 3, we need all entries of the similarity matrix \mathbf{A} . Hence, we cannot rely *only* on examples in every microbatch i -th to compute the microbatch gradients c_i 's. Second, GradAccum must allocate memory for the cumulative gradient \bar{g} .¹ As \bar{g} has as many elements as θ , its memory grows as we scale up the networks F and G . This growth becomes a more pronounced issue as we scale up our models. For reference, our largest model has 3B weights, occupying roughly 11GB of accelerator memory. Spending another 11GB on \bar{g} , while possible, defeats the purpose of saving memory in GradAccum. In the remaining of this subsection, we discuss how to modify GradAccum so that we can use it to scale up contrastive learning.

4.2 Modifying Pipelining and GradAccum for the Contrastive Loss

Microbatching the contrastive loss. To enable proper GradAccum, a key observation is that while we need the entire similarity matrix \mathbf{A} to compute ContrastiveLoss_B in Equation 3, we do *not* need to store all the intermediate results leading to the matrix in memory. This observation immediately connects to re-materialization, which trades computation for memory by dropping some intermediate hidden states during the forward pass and re-computing them during back-propagation. Following this insight, we propose to combine re-materialization with gradient accumulation by microbatching the contrastive loss and re-materializing each microbatch.

Specifically, we first run a forward pass on the networks F, G to compute the entire similarity matrix \mathbf{A} while discarding all intermediate hidden states. Then, we use \mathbf{A} to compute ContrastiveLoss_B and the gradient $\nabla_{\mathbf{A}} \text{ContrastiveLoss}_B$ and microbatch this gradient along the batch axis. Finally, for each microbatch, we re-materialize the hidden states, *i.e.*, rerun the forward computation, and back-prop and accumulate the corresponding gradient microbatch of $\nabla_{\mathbf{A}} \mathcal{L}_c$ into the weights of the networks F, G .

Algorithm 1 presents this procedure in detail and provides the memory analysis for each step. As shown, our algorithm can compute the *exact* microbatch gradients from an entire batch of B examples, with the peak memory usage of $\Theta(M \cdot \max\{\text{Mem}(F), \text{Mem}(G)\})$, instead of $\Theta(B \cdot (\text{Mem}(F) + \text{Mem}(G)))$. We note

1. It is worth noting that this is a common issue with GradAccum and is not specific to contrastive learning.

Inputs	<ul style="list-style-type: none"> • Networks F, G with a weight vector $\theta = [\theta_F, \theta_G]$, • A minibatch of B (image, text) pairs $\{(\mathbf{x}_i, \mathbf{y}_i)\}_{i=1}^B$, • Microbatch size M. Assuming M evenly devices B. 	<ul style="list-style-type: none"> ▷ B is the contrastive batch size. ▷ M is the largest in-memory batch size. 	Memory Analysis
Yields	<ul style="list-style-type: none"> • Gradients ∇_{θ} ContrastiveLoss for B/M minibatches of the minibatch. 	<ul style="list-style-type: none"> ▷ The loss is computed as in Equation 3 	
1	Allocate embedding matrices $\mathbf{X}, \mathbf{Y} \in \mathbb{R}^{D \times B}$	▷ D is the embedding size	$\Theta(BD)$
2	For $i = 1$ to B/M do :	▷ Sequentially compute the embeddings for	
3	Let $J \leftarrow \{j : (i-1)M + 1 \leq j \leq iM\}$	microbatches of images and text sequences,	
4	$\mathbf{X}_{:,J} \leftarrow F(\mathbf{x}_J)$	<i>not</i> saving the activations of F and G .	$\Theta(M \cdot \text{Mem}(F))$
5	$\mathbf{Y}_{:,J} \leftarrow G(\mathbf{y}_J)$		$\Theta(M \cdot \text{Mem}(G))$
6	$\mathbf{A} \leftarrow (\mathbf{X}^{\top} \cdot \mathbf{Y}) / \tau$	▷ $\mathbf{A} \in \mathbb{R}^{B \times B}$ is the similarity matrix	
7	RowLoss $_B \leftarrow -\frac{1}{B} \sum_{i=1}^B \log \frac{\mathbf{A}_{i,j}}{\sum_{k=1}^B \mathbf{A}_{i,k}}$	▷ The contrastive loss in Equation 3	$\Theta(B^2)$
8	ColumnLoss $_B \leftarrow -\frac{1}{B} \sum_{j=1}^B \log \frac{\mathbf{A}_{i,j}}{\sum_{k=1}^B \mathbf{A}_{k,j}}$		
9	ContrastiveLoss $_B \leftarrow \frac{\text{RowLoss}_B + \text{ColumnLoss}_B}{2}$		
10	$d\mathbf{A} \leftarrow \text{BackProp}(\text{ContrastiveLoss}, \mathbf{A})$	▷ Back-prop to compute $\nabla_{\mathbf{A}}$	
11	$d\mathbf{X} \leftarrow \mathbf{Y} \cdot d\mathbf{A}$	▷ Because $\mathbf{A} = \mathbf{X}^{\top} \mathbf{Y}$	
12	$d\mathbf{Y} \leftarrow \mathbf{X} \cdot d\mathbf{A}$		
13	For $i = 1$ to B/M do :	▷ Repeat a forward pass on F, G to	
14	Let $J \leftarrow \{j : (i-1)M + 1 \leq j \leq iM\}$	back-prop the gradients from $d\mathbf{X}, d\mathbf{Y}$ to	
15	$d\theta_F \leftarrow \text{ForwardAndBackProp}(d\mathbf{X}_{:,J}, \theta_F)$	the weights θ_F, θ_G .	$\Theta(M \cdot \text{Mem}(F))$
16	$d\theta_G \leftarrow \text{ForwardAndBackProp}(d\mathbf{Y}_{:,J}, \theta_G)$		$\Theta(M \cdot \text{Mem}(G))$
17	Yield $d\theta = [d\theta_F, d\theta_G]$		

Algorithm 1: Pseudo code of our gradient accumulation process for the contrastive loss. Here $\text{Mem}(F)$, $\text{Mem}(G)$ denote the memory required for a pass for the networks F, G . As shown in our memory analysis, at the cost of repeating one forward pass for F, G (lines 13-16), our procedure’s peak memory footprint is dominated by $\Theta(M \cdot \max\{\text{Mem}(F), \text{Mem}(G)\})$.

that our algorithm can be flexibly modified to work different microbatch-sizes, *i.e.*, M , for the image network F and the text network G . This flexibility allows for more efficient computations, *e.g.*, when one network is smaller than another and thus, can operate with larger microbatches.

Accumulating the microbatch gradients. Algorithm 1 yields a stream of microbatch gradients $c_1, \dots, c_{B/M}$, which need to be accumulated, *i.e.*, averaged, into \bar{g} to perform the batch weight update. As discussed, we want to avoid allocating extra memory for \bar{g} . To do this, we need two assumptions about our training implementation. Our first assumption is that we use an optimizer which involves gradient moments (Nesterov, 1983; Tieleman and Hinton, 2012; Kingma and Ba, 2015; Loshchilov and Hutter, 2019; Shazeer and Stern, 2018). This assumption motivates our idea to avoid allocating \bar{g} : since the optimizer already allocates the memory for gradient moments, typically called *slots*, we will directly accumulate the microbatch gradients c_i ’s into these slots.

We illustrate this idea with Adam (Kingma and Ba, 2015), a popular optimizer that involves two gradient moments. At training step t , Adam receives the averaged minibatch gradient \bar{g} and makes the following updates to its gradient moments v_1 and v_2 :

$$\bar{g} = 1/B \cdot \sum_{i=1}^B g_i = 1/\underbrace{(B/M)}_K \cdot \sum_{i=1}^{B/M} c_i$$

$$v_1^{(t)} = \beta_1 v_1^{(t-1)} + (1 - \beta_1) \bar{g}$$

$$v_2^{(t)} = \beta_2 v_2^{(t-1)} + (1 - \beta_2) \bar{g}^2$$

Accumulating the microbatch gradients c_i 's to v_1 is straightforward. We can simply modify v_1 's single update with \bar{g} into $K = B/M$ updates as follows:

$$v_1 \leftarrow k_i v_1 + (1 - \beta_1) c_i, \text{ where } k_i = \begin{cases} \beta_1 & \text{if } i = 1 \\ 1/K & \text{otherwise} \end{cases}$$

Unfortunately, the same approach is not applicable for v_2 , as the square of the sum is generally different from the sum of the squares, *i.e.* $(\sum c_i)^2 \neq \sum c_i^2$. However, the difference between these two quantities turns out to be:

$$\underbrace{\frac{1}{K} \sum_{i=1}^K c_i^2}_{\text{sum of squares}} - \underbrace{\left(\frac{1}{K} \sum_{i=1}^K c_i \right)^2}_{\text{square of sum}} = \mathbf{E}[c_i^2] - \mathbf{E}[c_i]^2 = \mathbf{Var}[c_i],$$

which we can estimate. Indeed, since each c_i 's is the mean of M per-example gradients g_j 's in the i -th microbatch, we can treat c_i 's as the population mean of M observed examples drawn from a random variable $\mathbf{g} \sim \text{Uniform}\{g_1, \dots, g_B\}$. This treatment allows us to use the familiar identity:

$$\mathbf{Var}[c_i] = \mathbf{Var}\left[\frac{1}{M} \sum_{j=(i-1)M+1}^{iM} g_j\right] = \frac{\mathbf{Var}[\mathbf{g}]}{M} \quad (4)$$

Therefore, to estimate $\mathbf{Var}[c_i]$, we only need to estimate $\mathbf{Var}[\mathbf{g}]$. For this, we make the second assumption about our training: that we use a data parallelism setting with R replicas. Under this assumption, each microbatch gradient c_i is obtained from an all-reduce operation on R replicas, each of which processes M/R examples. Once again, treating these per-device gradients d_1, \dots, d_R as the population mean of M/R observed examples for \mathbf{g} , we can apply Identity 4 to obtain: $\mathbf{Var}[d] = \mathbf{Var}[\mathbf{g}] / (M/R)$. This treatment allows us to perform GradAccum while avoiding to allocate \bar{g} .

5. Batch Size Scaling with the Single-Program Multiple-Data (SPMD) Scheme

In Section 4, we have seen that one circumvent the memory bottleneck of large models and large batch sizes for image-text contrastive learning by: (1) ‘‘chunk’’ a large batch of B image-text pairs into arbitrarily smaller microbatches, (2) compute the gradient for each microbatch, and (3) accumulate them. While such an approach is generic and can work for any global contrastive batch size B and any microbatch size M , there are two steps in the approach that makes the resulting gradient *inexact*. The first inexact computation comes from the approximations when accumulating the microbatch gradients. This is a necessary tradeoff to avoid allocating the memory to accumulate the microbatch gradients. The second inexact computation is more subtle, and is specific to our modeling choice, and has also been noted by [Huang et al. \(2019\)](#). Specifically, when our networks F and G depend on the batch, *e.g.*, via the batch normalization layers in our image encoder F , then the outputs of the networks for multiple microbatches are generally different from those for one entire global batch. When the microbatch size M is too small compared to B , the discrepancies become very large and can cause the covariate shift in the image encoder F which was the original motivation for batch normalization. More recent image encoders can overcome such inexact computations because they avoid batch normalization by replacing it with layer normalization like Vision Transformer ([Dosovitskiy et al., 2021](#)), or just do not use any normalization at all like NFNet ([Brock et al., 2021](#)). However, the inexact gradient accumulation remains even for such models.

To overcome these inexact computations, in this section, we discuss an alternate approach to circumvent the memory bottleneck. This approach is based on the SPMD programming scheme. We find that not only does our SPMD method provide exact computations which lead to better results than pipelining and

GradAccum, but our SPMD method also has a better latency per training step. However, as we shall see in Section 5.1 and Section 5.2, our SPMD method requires several manual designs, which make it less generic than pipelining and GradAccum.

5.1 Weight Sharding

As model sizes grow, model weights occupy a significant part of accelerator memory. In modern optimizers for deep learning models, such as Adam (Kingma and Ba, 2015), RMSprop (Tieleman and Hinton, 2012), and AdamW (Loshchilov and Hutter, 2019), every weight tensor is additionally accompanied by the first and second gradient moments, hence tripling its memory footprint. Furthermore, in the vanilla data parallelism training, all these weights are replicated to *all* accelerators. In our experiments with a relatively large model size, roughly 4GB of accelerator memory is occupied by these weights and their gradient moments, which is significant for the typical 16GB memory in an accelerator in 2022, such as a Google TPU core or an Nvidia RTX 3080 GPU.

Here, we split the weight tensors in our encoder networks, *i.e.* F and G in Section 3, into multiple accelerator cores, and only combine these tensors together when the whole tensor is needed to perform certain computations. Note that upon splitting a weight tensor to multiple cores, we also split its first and second gradient moments in the similar way. Figure 1 illustrates our weight sharding strategy on the 2D convolution operation which is prevalent in image encoder models.

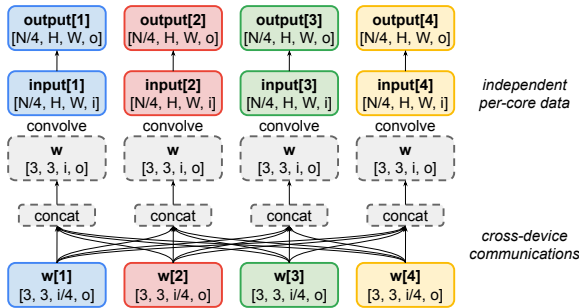


Figure 1: An illustrative example for our model parallelism design. Shown is 2D convolution operation with a 3x3 kernel sharded to 4 cores. Gray cells represent the tensor values that are mirrored across all cores, while cells of other colors represent per-core independent tensor values. The convolution’s input is a tensor of shape $[N, H, W, i]$ which is sharded along its first dimension so that each core has processes a tensor of shape $[N/4, H, W, i]$. The convolution’s kernel is a tensor of shape $[3, 3, i, o]$, but each core only stores one shard of the kernel which has size $[3, 3, i/4, o]$. Before convolving, every core receives the kernel shards from all other cores and concatenate the shares, forming the complete kernel of size $[3, 3, i, o]$. After convolving, the complete kernel is discarded from all cores’ memory.

Our approach is based on the Single-Program Multiple-Data (SPMD) technique, which has been successfully applied to train large language models in previous works such as in Xu et al. (2021); Lepikhin et al. (2020). In the SPMD technique, we define a computational graph which represents our entire training program. This computational graph is compiled once, and then is replicated identically to all computational cores to run the training program. While all of our computational cores run an identical program, they are allowed to receive different inputs and hence can produce different outputs. These inputs and outputs can be organized in certain ways to define arbitrarily complex model parallelism strategies. Next, we describe how we apply the SPMD technique on our *model weights* only.

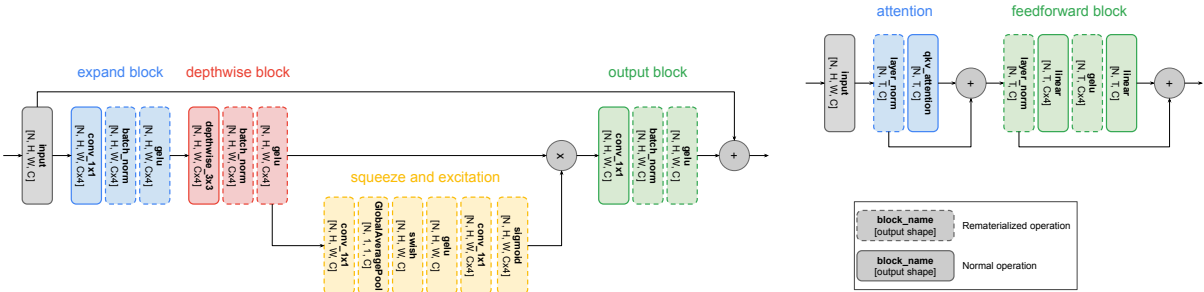


Figure 2: Generic rematerialization map for the blocks in our CoAtNet models. **Left:** in the Mobile Inverse Convolution blocks (MBCov), all batch normalization layers and activation layers, as well as all layers in the squeeze and excitation steps, are rematerialized. **Right:** in Transformer blocks, only the layer normalization layers and activation layers are rematerialized.

Our training program runs typically on a cluster of 2048 TPUv3 cores. We partition these 2048 cores into R replicas, each of which uses $2048/R$ cores. The value of R governs how the weights of our image encoder F and our text encoder G are stored in the memory of our 2048 cores. In particular, all weight tensors in the networks F and G are split into R equal parts, each lives in one of the R cores in a replica. Note that since we have $2048/R$ replicas, the weights of our image and text encoders are still replicated for $2048/R$ times. For instance, our cores 1^{st} , 2^{nd} , ..., R^{th} can each store $1/R$ of the weight tensors, and then the cores $R + 1^{\text{st}}$, $R + 2^{\text{nd}}$, ..., $2R^{\text{th}}$ store an identical copy of these tensors. Thus, using fewer replicas and more cores per replica leads to a better memory utilization, at a higher overhead for cross-cores communications. We empirically find that using 512 replicas and 4 cores per replica offers a good balance.

It is important to note that we only apply SPMD on our model weights, and not on any other steps of our computations. This means that if our training program receives an input batch of B examples, then these B examples are distributed equally to all our 2048 cores. In other words, each of our 2048 cores processes $B/2048$ examples, regardless of the value of R . We find that this design choice disentangles our weight sharding strategy from the rematerialization strategy, as described next in Section 5.2.

5.2 Rematerialization

The technique of rematerialization, also widely known as gradient checkpointing (Chen et al., 2016), preserves the accelerator memory while training neural networks. It works by *not* saving certain values from a network’s forward pass, and recompute them in the backward pass *only* when their values are needed for a particular calculation. For instance, if our image encoder F , as discussed in Section 3 has 100 layers, a rematerialization program can decide that after the forward pass, only the values of layers 10^{th} , 20^{th} , ..., 90^{th} are kept in an accelerator’s memory, while the values of other layers are removed. If all layers of F consumes similar memory, this rematerialization program has reduced the memory cost by 10 times, at the trade off that the values of the unsaved layers in the forward pass, such as layer 21^{st} or layer 72^{nd} , have to be recomputed in the backward pass.

We select which layer to rematerialize in our image encoder F and our text encoder G based on a simple heuristic. Ideally, we want to rematerialize the layers that are fast to recompute but consumes the more memory. Since we utilize weight sharding, as described in Section 5.1, the computations that involve weights are slower than normal because of their overhead time for cross-core communications. As such, we keep almost all layers that involve weights, such as convolution, attention, and dense feed-forwards,

in our accelerator’s memory. In contrast, layers that do not involve weights, such as activation functions, batch normalization, and layer normalization, are all rematerialized. Figure 2 illustrates our rematerialization strategy for all three block types in our image and text encoders: the mobile-inverse convolutional block (Tan and Le, 2019; Dai et al., 2021), the attention block, and the feed-forward blocks (Vaswani et al., 2017).

We find this design choice beneficial, because in modern encoder architectures, every layer that involves weights is typically followed by a normalization layer or an activation layer. As such, our design allows more than half of the encoder’s activation values to be removed from the accelerator’s memory after each forward pass, while leaving only the light computational steps to be repeated in each backward pass. We empirically find that weight sharding and rematerialization, each of our forward-backward pass is 1.4 times slower than the vanilla implementation of the same batch size.

Exceptions to our heuristics. Certain parts of our encoders do not follow these general heuristics, as we find that doing so saves a certain amount of time at the cost of using a little extra memory. Here, we describe these exceptions:

1. All weights in batch normalization and layer normalization in our models, including the β ’s and γ ’s and the moving average statistics of batch normalization, are *not* sharded. Instead, these weights are replicated to all computational cores to avoid cross-cores communications, because they are one dimensional vectors which do not occupy much memory.
2. All computations the Squeeze-and-Excitation blocks (SE; (Hu et al., 2018)) of our models are rematerialized, including the convolutions. This is because these SE blocks only involve 1x1 convolution with reduced internal channels, making them less costly to recompute. In addition, all the weights of these 1x1 convolutions are replicated to all of our cores, because they have a small memory footprint but are reused in the backward pass for rematerialization.

5.3 Comparison with Pipelining and Gradient Accumulation

We measure and compare the step time and peak memory usage of our SPMD approach and our Pipelining and GradAccum approach from Section 4. We measure these pieces of information as the contrastive batch size B becomes larger. In particular, we start with $B = 2^{16}$ and double B until we reach $B = 2^{20}$. When B increases, but our model can still fit into the our memory only with vanilla data parallelism, we measure the step time and the peak memory using this setting. These measures serve as the reference to quantify how much overhead is introduced by pipelining, SPMD, or rematerialization as a whole. When B grows and our models can no longer train with merely data parallelism, we experiment with the Pipelining and GradAccum, and compare the resulting programs with the SPMD programs of the same model and batch size. Note that for the pipelining approach, we set the microbatch size to the largest size that vanilla data parallelism can fit in our accelerator’s memory.

For all settings, we profile a model in 15 seconds. Our profiling tool tracks the time and memory usage of our models during their forward and backward passes in each step. Note that our backward pass time *includes* the time our models spend on their rematerialized computations (as discussed in Section 5.2), as these computations happen while the models compute their gradients. Note that other than these forward and backward passes, every step of our models has some extra overheads for miscellaneous computations that are not recorded by our profiling tool, *e.g.*, gradient clippings and updating model parameters.

All of our measurements are reported in Table 2. From the table, it can be seen that our model parallelism strategy leads to a faster overall step time, compared to the pipelining approach in the same setting. Breaking down these step times, it can be seen that the run time of our strategy’s model forward pass is very close to

Model Size	Methods	Batch (B)	Step time (milliseconds)			Memory (GB)
			FWD	BWD	Total	
Small	Data parallelism	2^{16}	28.6	81.2	128.5	4.2
	Data parallelism	2^{17}	65.8	144.5	230.3	6.4
	Data parallelism	2^{18}	131.2	282.9	428.0	9.9
	Data parallelism	2^{19}	261.0	559.4	842.4	14.8
	Data parallelism	2^{20}	—	—	—	OOM
	Pipeline & GradAccum	2^{20}	301.7	1497.4	1983.1	11.2
	SPMD	2^{20}	271.8	1311.8	1631.6	15.2
Medium	Data parallelism	2^{16}	129.5	270.8	437.6	10.7
	Data parallelism	2^{17}	237.7	536.4	806.1	13.8
	Data parallelism	2^{18}	—	—	—	OOM
	Pipeline & GradAccum	2^{18}	597.7	1677.1	2677.3	12.6
	SPMD	2^{18}	599.3	1407.2	2018.6	12.1
	Pipeline & GradAccum	2^{19}	1393.1	4087.8	5601.2	12.8
	SPMD	2^{19}	1402.7	3141.1	4912.3	14.1
	Pipeline & GradAccum	2^{20}	3014.3	6129.9	9781.4	12.6
	SPMD	2^{20}	2909.7	4912.3	8361.1	15.4

Table 2: Comparison between our SPMD programs and our Pipelining & GradAccum programs. Shown are the step times and memory footprints of our small-sized and medium-sized models at different batch sizes. With the same model size and batch size, our SPMD design results in a larger device memory footprint and Pipelining & GradAccum, but SPMD is faster.

the run time of pipelining’s forward pass, but our backward time is often a lot faster. For instance, in our largest setting, with the medium-sized model and the contrastive batch size $B = 2^{20}$, our backward time is more than 1.2 seconds faster than that of the pipelining approach, amounting to about 10% of the total step time. Additionally, our strategy also has a faster total step time, perhaps because do not need to spend extra time to accumulate the microbatch gradients like the pipelining approach.

Finally, we note that as B grows larger, the SPMD approach typically occupies more accelerator memory than does the pipelining approach. This is because in the pipelining approach, increasing the contrastive batch size B only leads to more microbatches, but does not change the micro batch size, and so the accelerator’s memory remains constant. As such, the pipelining approach is still applicable if B grows larger than 2^{20} , but the SPMD strategy has to be redesigned, *e.g.* by deciding to rematerialize a larger portion of our image and text encoder.

6. Theoretical Insight on the Role of Contrastive Batch Size

In this section, we provide a theoretical insight that increasing the contrastive batch size tends to improve the performance of the final model, which motivates and partially justifies the design of our new algorithm in the previous section. Let $\hat{y}_1, \dots, \hat{y}_B$ be the sequence of the text sentence inputs used in training. Similarly, let $\bar{y}_1, \dots, \bar{y}_M$ be the sequence of the text sentence inputs used in testing. We then define the normalized training loss by

$$\hat{\ell}_B(x, y) = -\frac{B \exp(F(x)^\top G(y))}{\sum_{k=1}^B \exp(F(x)^\top G(\hat{y}_k))} = -\frac{\exp(F(x)^\top G(y))}{\frac{1}{B} \sum_{k=1}^B \exp(F(x)^\top G(\hat{y}_k))},$$

where we multiply B to scale the loss correctly in the regime of $B \rightarrow \infty$. That is, since the unnormalized loss goes to zero ($\hat{\ell}_B(x, y)/B \rightarrow 0$) as the batch size approach infinity ($B \rightarrow \infty$), analyzing the unnormalized version of the loss $\hat{\ell}_B(x, y)/B$ can mistakenly predict benefits of the large contrastive batch size. We avoid this with the normalization. Similarly, we define the normalized testing loss by

$$\bar{\ell}_M(x, y) = -\frac{\exp(F(x)^\top G(y))}{\mathbb{E}_{\bar{y}}[\exp(F(x)^\top G(\bar{y}))]}.$$

Then, the prediction at testing time for a new input x is given by

$$\text{pred}(x) = \underset{j \in \{1, 2, \dots, M\}}{\text{argmax}} F(x)^\top G(\bar{y}_j) = \underset{j \in \{1, 2, \dots, M\}}{\text{argmin}} \bar{\ell}_M(x, \bar{y}_j).$$

Therefore, $\hat{\ell}_B(\hat{x}_i, \hat{y}_i)$ is minimized during training for training points (\hat{x}_i, \hat{y}_i) while we want to minimize $\bar{\ell}_M(x, y)$ to make a prediction at a new point x . This leads to the question of the generalization from training to unseen-data, which can be studied by analyzing the upper bound on the following quantity:

$$\mathbb{E}_{x, y}[\bar{\ell}_M(x, y)] - \hat{\mathbb{E}}_S[\hat{\ell}_B(x, y)],$$

where $\hat{\mathbb{E}}_S[\hat{\ell}_B(\hat{x}, \hat{y})]$ is the empirical training loss with a dataset, $S = ((\hat{x}_i, \hat{y}_i))_{i=1}^m$, of size m . To analyze this in a statistical setting, we define a vector $v \in \mathbb{R}^D$ by $v_i = F(x)_i - \frac{\sum_{k=1}^B \exp(F(x)^\top G(\hat{y}_k)) G(\hat{y}_k)_i}{\sum_{k=1}^B \exp(F(x)^\top G(\hat{y}_k))}$ for all $i \in \{1, \dots, D\}$, and assume that $\hat{y}_1, \hat{y}_2, \dots, \hat{y}_B \stackrel{iid}{\sim} p_y$, $\bar{y}_1, \bar{y}_2, \dots, \bar{y}_M \stackrel{iid}{\sim} p_y$, $\exp(F(x)^\top G(y)) \leq c_1$, $\hat{\ell}_B(x, y) \leq c_2$, $\|F(x)\|_2 \leq c_3$, $\frac{\exp(F(x)^\top G(y))}{\frac{1}{B} \sum_{k=1}^B \exp(F(x)^\top G(\hat{y}_k))} \leq c_4$, $\|F(x_i)\|_2 \leq c_5$, $\|v\|_2 \leq c_6$, $\|y\|_2 \leq c_7$, and $\|x\|_2 \leq c_8$, with probability one. Moreover, by defining $\gamma(x) = \mathbb{E}_{\bar{y}}[\exp(F(x)^\top G(\bar{y}))] - \frac{1}{B} \sum_{k=1}^B \exp(F(x)^\top G(\hat{y}_k))$, we assume that γ is c_9 -Lipschitz; i.e., $|\gamma(x) - \gamma(x')| \leq c_9 \|x - x'\|_2$ for all $x \in \mathcal{X} \subseteq \mathbb{R}^k$. To provide a concrete insight, we consider standard deep neural networks, of the form

$$\begin{aligned} G(y) &= (\omega_L \circ \sigma_{L-1} \circ \omega_{L-1} \circ \sigma_{L-2} \cdots \sigma_1 \circ \omega_1)(y), \\ F(x) &= (\omega'_{L'} \circ \sigma'_{L'-1} \circ \omega'_{L'-1} \circ \sigma'_{L'-2} \cdots \sigma'_1 \circ \omega'_1)(x), \end{aligned}$$

where $\omega_l(q) = W_l q$ represents the linear transformation and σ_l is an element-wise nonlinear activation function. Similarly, $\omega'_l(q) = W'_l q$ and σ'_l is an element-wise activation function.

The following theorem provides an insight on the role of the contrastive batch size to close the accuracy gap from contrastive models to their supervised counterparts:

Theorem 1 *Suppose that the activation functions σ and σ'_l are 1-Lipschitz and positive homogeneous for all $l \in [L - 1]$. Let $\mathcal{G} = \{y \mapsto G(y) : (\forall l \in [L - 1])[\|W_l\|_F \leq M_l] \wedge \|(W_L)_k\|_F \leq M_{L,k}\}$ and $\mathcal{F} = \{x \mapsto F(x) : (\forall l \in [L' - 1])[\|W'_l\|_F \leq M'_l] \wedge \|(W'_{L'})_k\|_F \leq M'_{L',k}\}$ where $(W_l)_k$ is the k -th row of W_l . Then, for any $\delta > 0$, with probability at least $1 - \delta$, the following holds for all $F \in \mathcal{F}$ and $G \in \mathcal{G}$:*

$$\mathbb{E}_{x, y}[\bar{\ell}_M(x, y)] - \hat{\mathbb{E}}_S[\hat{\ell}_B(x, y)] \leq \frac{Q_1}{\sqrt{m}} + \frac{Q_2}{\sqrt{2B}} + c_2 \sqrt{\frac{\ln(2/\delta)}{2m}},$$

where $Q_1 = 2\sqrt{2}c_4\sqrt{c_5^2 + c_6^2}(\tilde{Q}_{1,1} + \tilde{Q}_{1,2})$, $Q_2 = c_1\mathbb{E}_{x,y}[A(x,y)](\tilde{Q}_{2,1} + \tilde{Q}_{2,2})$,

$$\begin{aligned}\tilde{Q}_{1,1} &= c_7(\sqrt{2\log(2)L} + 1) \left(\prod_{l=1}^{L-1} M_l \right) \left(\sum_{k=1}^D M_{L,k} \right), \\ \tilde{Q}_{1,2} &= c_8(\sqrt{2\log(2)L'} + 1) \left(\prod_{l=1}^{L'-1} M'_l \right) \left(\sum_{k=1}^D M'_{L',k} \right), \\ \tilde{Q}_{2,1} &= 2\sqrt{2}c_8c_9 + c_1\sqrt{\kappa \ln(\sqrt{\kappa B}/\delta)}, \\ \tilde{Q}_{2,2} &= 2\sqrt{2}c_3c_7(\sqrt{2\log(2)L} + 1) \left(\prod_{l=1}^{L-1} M_l \right) \sqrt{\sum_{k=1}^D M_{L,k}^2},\end{aligned}$$

$$\text{and } A(x,y) = \frac{\exp(F(x)^\top G(y))}{\left(\frac{1}{B} \sum_{k=1}^B \exp(F(x)^\top G(\hat{y}_k))\right) \mathbb{E}_{\tilde{y}}[\exp(F(x)^\top G(\tilde{y}))]}.$$

Proof The proof is presented in Appendix H. ■

Theorem 1 shows that the generalization gap $\mathbb{E}_{x,y}[\bar{\ell}_M(x,y)] - \hat{\mathbb{E}}_S[\hat{\ell}_B(x,y)]$ approaches zero as the number of samples m and the contrastive batch size B increase, at the rate of $O(\frac{1}{\sqrt{m}} + \frac{1}{\sqrt{B}})$, with high probability. This shows the importance of the contrastive batch size B with the weak supervision setting without explicit labels: i.e., if B is small, the generalization gap can be large, even with a lot of training samples with large m . This is different from a classification task with a standard supervision, where a large m is sufficient to reduce the generalization gap. In sum, Theorem 1 provides the insight that we should increase both the number of samples m and the contrastive batch size B to improve the performance of the final model via the weekly supervised contrastive learning.

For general models beyond the standard deep neural networks, the following theorem provides a similar insight on the importance of the contrastive batch size:

Theorem 2 *Let \mathcal{F} be a set of maps $x \mapsto F(x)$ and \mathcal{G} be a set of maps $y \mapsto G(y)$. Then, for any $\delta > 0$, with probability at least $1 - \delta$, the following holds for all $F \in \mathcal{F}$ and $G \in \mathcal{G}$:*

$$\mathbb{E}_{x,y}[\bar{\ell}_M(x,y)] - \hat{\mathbb{E}}_S[\hat{\ell}_B(x,y)] \leq \frac{C_1}{\sqrt{2B}} + c_2\sqrt{\frac{\ln(2/\delta)}{2m}} + C_2 \sum_{k=1}^D (\mathcal{R}_m(\mathcal{F}_k) + \mathcal{R}_m(\mathcal{G}_k)) + C_3\tilde{\mathcal{R}}_B(G),$$

where $\mathcal{R}_m(\mathcal{H}) := \mathbb{E}_{S,\xi}[\sup_{h \in \mathcal{H}} \frac{1}{m} \sum_{i=1}^m \xi_i h(x_i, y_i)]$, $\mathcal{F}_k = \{x \mapsto F(x)_k : F \in \mathcal{F}\}$, $\mathcal{G}_k = \{y \mapsto G(y)_k : G \in \mathcal{G}\}$, $\tilde{\mathcal{R}}_B(G) = \mathbb{E}_{y,\xi} \left[\sup_{G \in \mathcal{G}} \frac{1}{B} \left\| \sum_{i=1}^B \xi_i G(y_i) \right\|_2 \right]$, $C_1 = c_1\mathbb{E}_{x,y}[A(x,y)]\tilde{Q}_{2,1}$, $C_2 = 2\sqrt{2}c_4\sqrt{c_5^2 + c_6^2}$, and $C_3 = 2c_1c_3\mathbb{E}_{x,y}[A(x,y)]$. Here, ξ_1, \dots, ξ_m are independent uniform random variables taking values in $\{-1, 1\}$.

Proof The proof is completed in Appendix H. ■

Similarly to Theorem 1, Theorem 2 shows that the gap $\mathbb{E}_{x,y}[\bar{\ell}_M(x,y)] - \hat{\mathbb{E}}_S[\hat{\ell}_B(x,y)]$ decreases as the number of samples m and the contrastive batch size B increase, at the rate of $O(\frac{1}{\sqrt{m}} + \frac{1}{\sqrt{B}})$, with high probability, for general models F and G . Because we are not specifying the types of the models F and G , we incur the additional terms that capture the model complexity of F and G : i.e., $\mathcal{R}_m(\mathcal{F}_k) + \mathcal{R}_m(\mathcal{G}_k)$ and $\tilde{\mathcal{R}}_B(G)$. The values of these model complexity terms differ for different models and typically scale as

$\mathcal{R}_m(\mathcal{F}_k) + \mathcal{R}_m(\mathcal{G}_k) = O(\frac{1}{\sqrt{m}})$ and $\tilde{\mathcal{R}}_B(G) = O(\frac{1}{\sqrt{B}})$ in terms of m and B as illustrated in the proof of Theorem 1 for standard deep neural networks. Therefore, it is desirable to use a large contrastive batch size, which motivates our new algorithm in the previous section.

7. Data and Model Scaling

7.1 Larger image-text dataset

Starting from the ALIGN dataset, which contains 1.7B weakly-aligned image-text pairs (Jia et al., 2021), we collect 5B more image-text pairs, hence expanding the dataset size by roughly 4 times. We acquire these 5B image-text pairs from the JFT dataset. In the JFT dataset, each image is associated with one or multiple classes. We convert these classes into a text sequence: “{class_1} and {class_2} and ... and {class_k}”. We combine the instances from JFT into ALIGN, forming our extended dataset, which we denote by ALIGN+JFT.

To tokenize the texts from ALIGN+JFT, we randomly sample 200M sentences and use them to train a sentence piece model (Kudo and Richardson, 2018) with a vocabulary size of 32K pieces. Using this tokenizer, we filter and discard the text sequences which are longer than 64 tokens. In our preliminary experiments, we find that using a tokenizer directly learned from ALIGN+JFT and adapting this filtering step can boost our top-1 accuracy on ImageNet ILSVRC-2012 by more than 1%.

7.2 Larger Model Architectures

We find that for the same computational budget, it is more beneficial to invest in scaling up the image encoder, rather than the text encoder. Thus, for our image encoder, we use the largest CoatNet architecture (Dai et al., 2021) due to its proven large learning capacity. This network has convolution layers followed by attention layers. For our text encoder, we use a simple transformer (Vaswani et al., 2017). Unlike ALIGN (Jia et al., 2021) which extracts the final text representations using a [CLS] token similar to BERT (Devlin et al., 2018), we average the representations across all steps at the top layer of our transformer.

By experimenting with the scaling benefits for small models and generalizing these findings to larger models, we choose three model sizes, termed BASIC- $\{S,M,L\}$ for Small, Medium, and Large. In Appendix A, we report our architectures and their computational costs and provide a small-scale study on the effects of scaling model sizes.

8. Pretraining and Finetuning

To further speed up the training of our networks, we make use of pretraining. In our experiments, we first pretrain the image encoder on a large labeled dataset using the standard softmax classification loss. After pretraining the image encoder, we fix all of its weights and just train the text encoder using contrastive learning. Compared to contrastive learning with GradAccum, the pretraining-finetuning procedure is much more efficient in terms of peak memory usage. This is because we never have to compute the gradients of *both* the image encoder and the text encoder, which allows automated compiler optimizations to free up unused memory on-the-fly.

Despite its reduced memory usage, we find that this pretraining-finetuning scheme has a weakness: it never exposes the image encoder to noisy image-text data, which makes the image encoder fail on certain tasks. For instance, while some pretrained-and-finetuned models achieve similar accuracy to their contrastive counterparts on ImageNet or CIFAR, they completely fail on an easier task – MNIST. This is because our pre-

training labeled dataset, which mostly consists of natural images, has very few digit images. Meanwhile, our noisy image-text dataset has plenty instances that can teach a model certain optical character recognition skills.

As will be shown in Section 9, our best experimental results are achieved using a hybrid procedure. First, we pretrain the image encoder on a large labeled dataset, then fix its weights and train the text encoder using the contrastive loss on our image-text dataset. Finally, we finetune both image and text encoders, using our GradAccum technique when needed. In Section 10, we present ablation studies to analyze the effects of pretraining, finetuning, and other alternative training procedures.

9. Experiments

9.1 Training details

Labeled data for pretraining. For pretraining (Section 8), we use the JFT dataset. This dataset has been used in previous publications (Zhai et al., 2021; Dosovitskiy et al., 2021; Kolesnikov et al., 2020), but it has been constantly expanded. The JFT version used in our experiments has 5B images, each of which can be associated to one or multiple labels out of 29K possible classes.

Data filtering. A problem with training on large auto-curated datasets like ALIGN and JFT is that these datasets might unintentionally contain examples from our test sets. To avoid such contaminations, we filter all instances in our training data that has a structural similarity index (SSIM (Wang et al., 2004)) of at least 0.5 with any image from our evaluation benchmarks.

Optimizer. We train our models with our own optimizer called AdaFactorW, adapted from two existing ones: AdaFactor (Shazeer and Stern, 2018) and AdamW (Loshchilov and Hutter, 2019). Specifically, we factorize our second gradient moments like AdaFactor, and decouple the weight decay from all moments like AdamW. To further save memory, we follow Zhai et al. (2021) and store the first gradient moments in `bfloat16`. We observe, however, that while we can *store* these moments in `bfloat16`, we need to convert them into `float32` prior to computing our weight updates to avoid numerical instability.

Datasets	Birdsnap	Caltech101	CIFAR10	CIFAR100	DTD	EuroSAT	Flowers	Food101	ImageNet	MNIST	IIIT-Pets	PCam	RESISC45	STL10	SUN397	UCF101	VOC2007
ResNet-50	32.6	82.1	75.6	41.6	41.7	41.1	65.9	81.1	59.6	66.6	85.4	57.6	54.2	94.3	59.6	63.6	82.1
BASIC-S	38.6	91.6	86.4	57.8	54.3	29.1	76.8	86.0	71.9	32.4	93.2	54.3	53.5	96.7	67.3	65.5	83.4
	(+6.0)	(+9.5)	(+10.8)	(+16.2)	(+12.6)	(-12.0)	(+10.9)	(+4.9)	(+12.3)	(-34.2)	(+7.8)	(-3.3)	(-0.7)	(+2.4)	(+7.7)	(+1.9)	(+1.3)
ViT-B/16	39.1	89.3	91.6	68.7	46.0	54.1	70.4	89.2	68.6	56.0	88.9	48.1	65.5	98.2	65.2	69.8	83.9
BASIC-M	49.4	94.2	94.8	72.2	60.2	39.5	86.0	92.3	81.5	33.6	95.3	58.3	65.4	99.3	72.9	77.4	84.2
	(+10.3)	(+4.9)	(+3.2)	(+3.5)	(+14.2)	(-14.6)	(+15.6)	(+3.1)	(+12.9)	(-22.4)	(+6.4)	(+10.2)	(-0.1)	(+1.1)	(+7.7)	(+7.6)	(+0.3)
ViT-L/14-336	49.5	92.8	95.7	77.5	55.7	59.6	78.3	93.8	76.2	88.3	93.5	63.0	71.7	99.4	68.4	76.9	84.3
BASIC-L	59.2	94.7	97.5	82.3	64.6	51.0	91.2	95.1	85.7	40.3	97.9	59.6	72.7	99.6	76.2	84.8	84.6
	(+9.7)	(+1.9)	(+1.8)	(+4.8)	(+8.9)	(-8.6)	(+13.1)	(+1.3)	(+9.5)	(-48.0)	(+4.4)	(-3.4)	(+1.0)	(+0.2)	(+7.8)	(+7.9)	(+0.3)

Table 3: Performances of BASIC and CLIP models (Radford et al., 2021) on 17 image classification benchmarks. The first two blocks compare models of similar numbers of weights and FLOPs. The last block compares the largest CLIP and BASIC models.

Other hyperparameters. For all experiments, we train and evaluate with the image resolution of 224x224. While we can increase this resolution to gain performance (Tan and Le, 2019, 2021; Touvron et al., 2019; Radford et al., 2021; Jia et al., 2021), we choose not to do this and instead, reserve our computational resources for scaling up our model and our batch size. All of our other hyper-parameters can be found in Appendix B.

9.2 Results on Image Classification Benchmarks

We first present the zero-shot transfer performance of our BASIC models. We compare our models BASIC-{S,M,L} to CLIP models with similar computational budgets (Radford et al., 2021) on 17 natural image classification datasets. Details about these datasets can be found in Appendix C.

Zero-shot transfer models require textual prompts, which we take from CLIP (Radford et al., 2021) for consistent comparison. We suspect that using prompts which are tuned for our models can further improve our results as shown in (Lester et al., 2021), because the text sequences in our training data have a different distribution from the text sequences in CLIP.

Table 3 shows the comparison. From the table, it can be seen that BASIC models conclusively outperform CLIP models of the same computational budgets. Specifically, BASIC models demonstrate higher accuracy than CLIP models on 13 out of 17 datasets. On the Oxford IIIT Pets dataset, BASIC-L achieves 97.9% mean per-class recall which sets a new state-of-the-art, despite having never seen any training images from the dataset. On the other hand, BASIC models have low accuracy on EuroSAT, MNIST, and PCam. MNIST is where BASIC models perform worst, where the highest accuracy is only 40.3%. We discuss these failure cases further in Section 11.

9.3 Results on Robustness Benchmarks

Despite the convincing accuracy of modern deep learning models on ImageNet, concerns have been raised about their robustness (Szegedy et al., 2013). These concerns arise from a common failure mode of ImageNet-trained models: subtle changes to their input images, which are imperceptible to humans, can wildly alter their predictions with high confidence, *e.g.*, from “golden retriever” into “goldfish”.

In CLIP, Radford et al. (2021) have studied certain aspects of this failure mode. They have not drawn a definitive conclusion whether to attribute such failures to deep learning, ImageNet, or a combination of them. Instead, they cautioned against generalizing “too far from [their] initial findings”.

Here we advance CLIP’s study on the robustness of zero-shot models in two aspects. First, we analyze our BASIC models presented previously in Section 9.2 and reaffirm that zero-shot models are indeed more robust than their ImageNet-trained counterparts. Second, we perform an experiment which suggests that ImageNet’s labeled training examples *might be* responsible for making ImageNet-trained models less robust. Similar to CLIP’s authors, we caution readers that our experiment presents a correlation, not a causal analysis. In other words, we do not attribute the lack of robustness in ImageNet-trained models to the dataset.

More accurate zero-shot transfer models are also more robust. We evaluate BASIC-{S,M,L} models from Section 9.2 on 5 robustness benchmarks derived from ImageNet: ImageNet-A (Hendrycks et al., 2021b), ImageNet-R (Hendrycks et al., 2021a), ImageNet-V2 (Recht et al., 2019), ImageNet-Sketch (Wang et al., 2019), and ObjectNet (Barbu et al., 2019). These benchmarks have images in all or a subset of the 1000 ImageNet classes, but their inputs are selected from certain natural distribution shifts, which can cause ImageNet-trained models to make many more mistakes. Our numerical results are highlighted in Table 1 from Section 1. To visualize the data trend, in Figure 3, we plot the accuracy of zero-shot models – BASIC, CLIP (Radford et al., 2021), and ALIGN (Jia et al., 2021) – and of 200 ImageNet-trained models collected by Taori et al. (2020).

The data points from our BASIC models extend the prediction from CLIP: zero-shot transfer models have a higher *effective robustness* (Radford et al., 2021; Taori et al., 2020), *i.e.* they have higher robustness than ImageNet-trained models with the same ImageNet accuracy. To extrapolate from this trend, we fit a logistic curve (red dashes) to the zero-shot accuracy and robustness of zero-shot transfer models. The plot shows that this line meets the ideal robustness line at about 91% on the x-coordinate. In other words, our plot predicts

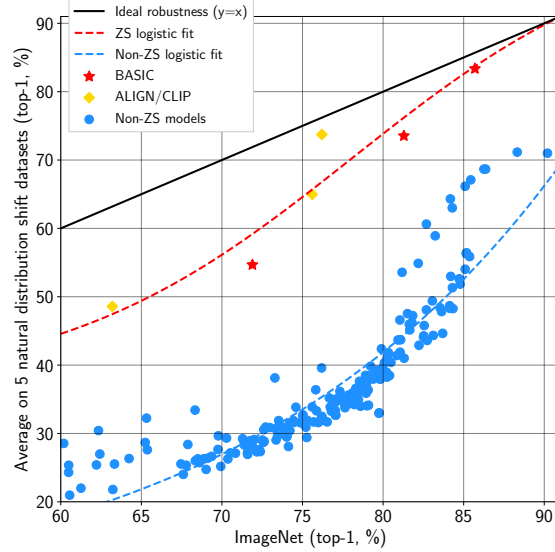


Figure 3: Top-1 accuracy on ImageNet vs. average top-1 accuracy on 5 robustness benchmarks. Zero-shot models (red stars and yellow rhombuses) have significantly higher effective robustness (Taori et al., 2020) compared to ImageNet-trained models (blue dots).

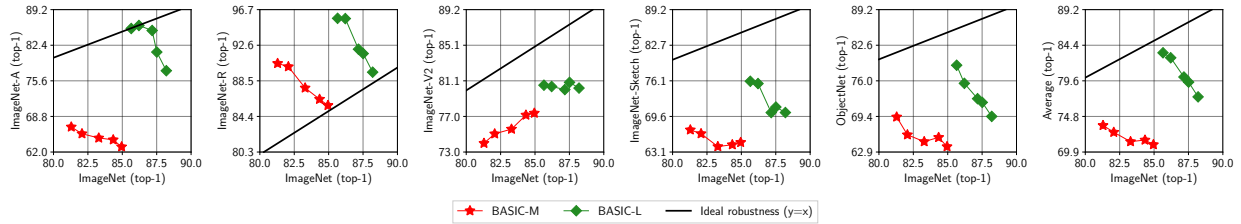


Figure 4: Top-1 accuracy of BASIC models on ImageNet and on 5 robustness benchmarks. In all cases, as the BASIC models are trained on more ImageNet labeled data (1%, 10%, 20%, and 50%), their ImageNet accuracy significantly increase, but their accuracy on the robustness benchmarks increase much less, or decrease.

that a model which achieves about 91% *zero-shot* accuracy on ImageNet, *i.e.*, just slightly better than the state-of-the-art ImageNet-trained model (Dai et al., 2021), will also achieve the ideal robustness.

ImageNet-finetuned models are less robust. We now study the effect of ImageNet’s labeled data on our models. We take the converged BASIC- $\{S,M,L\}$ checkpoints from Section 9.2 and continue to train them on 1%, 10%, 20%, and 50% of ImageNet’s labeled examples. Note that we continue training these checkpoints using the contrastive loss, where the names of ImageNet classes are utilized as text sequences accompanying their images. This is different from CLIP’s linear probing approach, which we do not perform to avoid potential confounding factors from our study, *e.g.* linear classifiers might behave differently from our zero-shot transfer classifiers. We then compare the accuracy of these finetuned models on ImageNet and on the 5 robustness benchmarks. The results are visualized in Figure 4.

The figure shows a clear trend: as our model learns from *more* labeled ImageNet data, they become more accurate on ImageNet, but these gains do not carry over to the robustness benchmarks. Specifically, with the exception of ImageNet-V2, for which the accuracy of finetuned models stay the same (for BASIC-L) or slightly increase (for BASIC-M), for all other robustness benchmarks, the finetuned models suffer from

significant performance drops. In the extreme case, 3% accuracy gain on ImageNet leads to 8.3% accuracy drop for ImageNet-R.

What makes our finetuned models less robust? A quick glance at our results might lead to the superficial conclusion that our models have overfit, as our finetuning sets are a lot smaller than ALIGN and JFT. However, this overfitting theory does not explain the trend observed in Figure 4: training on *more* labeled ImageNet data makes our models *less* robust. We hope our observation invites further causal analysis on the effects of ImageNet’s labeled data.

10. Ablation Study

10.1 The Importance of Batch Size Scaling

To demonstrate the role of large batch sizes, we conduct several controlled experiments for BASIC-S and BASIC-M on ALIGN. For both BASIC-S and BASIC-M, we fix all hyperparameters as shown in Table 6, but vary the batch size and the number of training steps. Models that are trained with larger batch sizes are trained with fewer steps to guarantee that they “see” the same number of examples. Table 4 presents the ImageNet top-1 zero-shot accuracy of all models at the end of their training, and Figure 5 visualizes their entire validation accuracy curves.

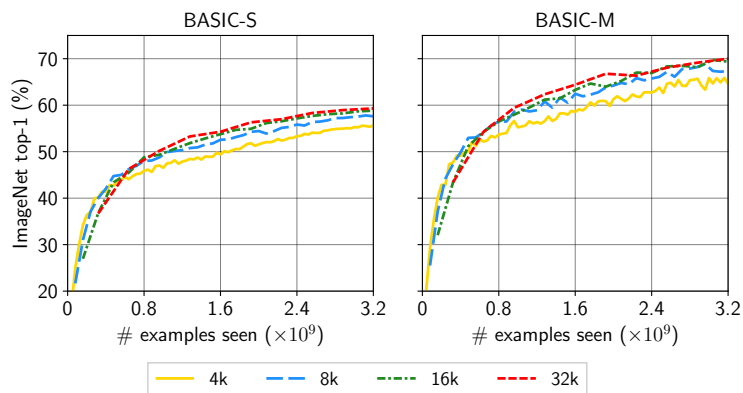


Figure 5: ImageNet held-out validation accuracy curves with different batch sizes. Models with smaller batch sizes are trained for more steps to ensure a fair comparison. The comparison shows that despite seeing the same number of training examples, models with larger batch sizes reach higher performances than models with more training steps. Image best viewed in color.

Batch size	Steps	BASIC-S	BASIC-M
4096	800K	55.6	64.8
8192	400K	57.6	67.7
16384	200K	58.8	69.4
32768	100K	59.3	70.1

Table 4: Top-1 ImageNet accuracy at the end of the training for our BASIC- $\{S,M\}$ models trained with different batch sizes and numbers of training steps. All models are trained for the same number of epochs, but models trained with larger batch sizes has a higher accuracy.

Table 4 and Figure 5 both suggest that training for more steps cannot equalize the benefit of large batch sizes. This phenomenon is consistent with the observation from SimCLR (Chen et al., 2020a,b): large batch sizes help contrastive learning. SimCLR observes that the benefit of large batch sizes saturate at 8192. In contrast, our results in Table 4 and Figure 5 show that larger batch sizes continue to benefit our models until 32768, and even until 65536 as in Section 9.2. We suspect that the benefits for large batch sizes do not saturate because our dataset size and model size are both larger than those of SimCLR, *e.g.* ALIGN with 1.7B examples compared to ImageNet with 1M examples, and BASIC- $\{S, M\}$ compared to ResNet- $\{50,101,152\}$. This comparison suggests the benefits of our method – combined scaling.

10.2 Data Scaling, Model Scaling, and Pretraining

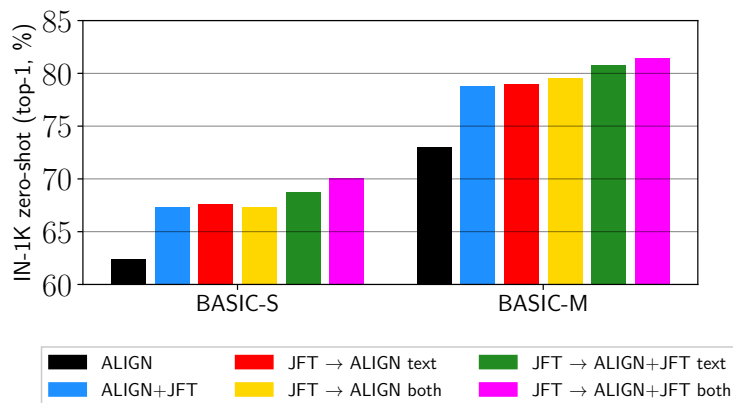


Figure 6: Break-down contributions of data scaling and model scaling for BASIC-S and BASIC-M. Shown are the ImageNet top-1 accuracy of our BASIC- $\{S,M\}$ models under different training settings. Models trained from scratch on ALIGN+JFT has almost the same performance with models pretrained on JFT and then finetuned on ALIGN or on ALIGN+JFT. Models that are pretrained and then have both their image and text encoders finetuned reach the highest accuracy. Figure best viewed in color.

We now study the benefits of other scaling dimensions, data and model scaling, on the quality of our models. We also study pretraining as an alternate training procedure to contrastive learning. We train BASIC- $\{S,M\}$ models in 6 different settings and plot their final top-1 ImageNet accuracy in Figure 6. Below, we compare and analyze the settings.

First, BASIC-S and BASIC-M respectively gain 5.3% and 5.8% accuracy when we expand the contrastive training dataset from ALIGN to ALIGN+JFT. These gains, albeit large, are smaller than the gain by enlarging the model size, *e.g.*, 11.7% when going from BASIC-S to BASIC-M.

Next, we study the effects of pretraining image encoders on JFT. As can be seen from Figure 6, models whose image encoders are pretrained on JFT and whose text encoders are subsequently trained on ALIGN, *i.e.*, the red bars, have similar performances with models trained from scratch on ALIGN+JFT, *i.e.*, the blue bars. Their similar accuracy suggest that the training losses – softmax cross-entropy or contrastive – have a much smaller effect than the datasets. In other words, when given the same dataset, the image encoders in BASIC models learn to become equally good, regardless of their loss functions.

To our surprise, training the text encoders for JFT-pretrained image encoders *on* ALIGN+JFT gains 1% for BASIC-S and 1.8% for BASIC-L, compared to training these text encoders on ALIGN. We suspect that these gains come from better representations for the textual prompts, since the models trained on ALIGN+JFT also sees the textual prompts which consist of clean JFT class names. However, this speculation needs a more thorough study to understand.

Finally, we find that if we take a converged model whose image encoder is pretrained on JFT and whose text encoder is trained on ALIGN+JFT, then we continue to train *both* its image encoders and text encoders at a small learning rate. This extra training phase gains us 1.4% ImageNet accuracy for BASIC-S, 0.6% for BASIC-M, and 0.4% for BASIC-L (not shown in this section).

11. Limitations

Despite the strong results of our zero-shot transfer classifier, especially on natural image classification tasks, they inevitably have their shortcomings. In this section, we discuss the problems that we find with our BASIC models.

Zero-shot transfer models do not perform well on test sets that are underrepresented in the training datasets. We emphasize the failures of BASIC on two test sets where BASIC models are much worse than CLIP models: EuroSAT, MNIST, PatchCamelyon (PCam) (see Table 3 from Section 9.2). Here, we summarize that BASIC models fail on MNIST and PCam because our training datasets ALIGN and JFT have relatively few images of handwritten digits and of lymph nodes, which are the domain of these datasets. Compared to MNIST and PCam, BASIC models do better on EuroSAT which consist of satellite land images, but their accuracy is lower than that of CLIP models. This is because the class names for these satellite images are not very descriptive to BASIC models. More analysis for these failures are in Appendix G.

Zero-shot transfer requires prompt engineering. In this paper, we use the prompts from CLIP (Radford et al., 2021) to make our results comparable to previous works. In Appendix G, we present examples which show that prompts that are badly chosen or adversarially chosen can hurt the accuracy of zero-shot transfer models by flipping their predictions. These examples suggest that prompt engineering is an important research topic to make zero-shot transfer models robust and reliable, but the topic is out of the scope of this paper.

Combined scaling is expensive. As reported in Appendix E, the hardware and training time for our models are not small. Despite the training cost, we can use the models in this paper without any finetuning, and hence avoid the finetuning cost. We hope that future research can reduce our models’ training expense, e.g., larger accelerator memory can save the extra re-materialization steps.

12. Conclusion

Zero-shot transfer learning represents a new paradigm where pretrained models can be used directly for downstream applications without collecting any application-specific data. However, in order to become practical for real-world applications, zero-shot transfer models need to bridge the accuracy gap to supervised and semi-supervised models.

In this paper, we presented combined scaling techniques that significantly boost the performance of zero-shot transfer models. We show that scaling in the data size, the model size, and the batch size all improves the final model’s accuracy and robustness. To overcome the memory limit arising from combined scaling, we devise a simple gradient accumulation method based on re-materialization.

References

- Martín Abadi, Paul Barham, Jianmin Chen, Zhifeng Chen, Andy Davis, Jeffrey Dean, Matthieu Devin, Sanjay Ghemawat, Geoffrey Irving, Michael Isard, et al. Tensorflow: A system for large-scale machine learning. In *OSDI*, 2016.
- Zeynep Akata, Florent Perronnin, Zaid Harchaoui, and Cordelia Schmid. Label-embedding for image classification. *IEEE TPAMI*, 2015a.
- Zeynep Akata, Scott Reed, Daniel Walter, Honglak Lee, and Bernt Schiele. Evaluation of output embeddings for fine-grained image classification. In *CVPR*, 2015b.
- Andrei Barbu, David Mayo, Julian Alverio, William Luo, Christopher Wang, Dan Gutfreund, Josh Tenenbaum, and Boris Katz. Objectnet: A large-scale bias-controlled dataset for pushing the limits of object recognition models. In *NeurIPS*, 2019.

Peter L Bartlett and Shahar Mendelson. Rademacher and gaussian complexities: Risk bounds and structural results. *Journal of Machine Learning Research*, 3(Nov):463–482, 2002.

Irwan Bello, William Fedus, Xianzhi Du, Ekin D Cubuk, Aravind Srinivas, Tsung-Yi Lin, Jonathon Shlens, and Barret Zoph. Revisiting resnets: Improved training and scaling strategies. In *NeurIPS*, 2021.

Thomas Berg, Jiongxin Liu, Seung Woo Lee, Michelle L Alexander, David W Jacobs, and Peter N Belhumeur. Birdsnap: Large-scale fine-grained visual categorization of birds. *CVPR*, 2014.

Lukas Bossard, Matthieu Guillaumin, and Luc Van Gool. Food-101—mining discriminative components with random forests. *ECCV*, 2014.

Andy Brock, Soham De, Samuel L Smith, and Karen Simonyan. High-performance large-scale image recognition without normalization. In *International Conference on Machine Learning*, pages 1059–1071. PMLR, 2021.

Jiacheng Chen, Hexiang Hu, Hao Wu, Yuning Jiang, and Changhu Wang. Learning the best pooling strategy for visual semantic embedding. In *CVPR*, 2021.

Tianqi Chen, Bing Xu, Chiyuan Zhang, and Carlos Guestrin. Training deep nets with sublinear memory cost. *Arxiv 1604.06174*, 2016.

Ting Chen, Simon Kornblith, Mohammad Norouzi, and Geoffrey E. Hinton. A simple framework for contrastive learning of visual representations. In *ICML*, 2020a.

Ting Chen, Simon Kornblith, Kevin Swersky, Mohammad Norouzi, and Geoffrey Hinton. Big self-supervised models are strong semi-supervised learners. In *NIPS*, 2020b.

Xinlei Chen, Haoqi Fan, Ross Girshick, and Kaiming He. Improved baselines with momentum contrastive learning. *ArXiv 2003.04297*, 2020c.

Yen-Chun Chen, Linjie Li, Licheng Yu, Ahmed El Kholy, Faisal Ahmed, Zhe Gan, Yu Cheng, and Jingjing Liu. Uniter: Universal image-text representation learning. In *ECCV*, 2020d.

Gong Cheng, Junwei Han, and Xiaoqiang Lu. Remote sensing image scene classification: Benchmark and state of the art. *Proceedings of the IEEE*, 2017.

Mircea Cimpoi, Subhansu Maji, Iasonas Kokkinos, Sammy Mohamed, and Andrea Vedald. Describing textures in the wild. In *CVPR*, 2014.

Adam Coates, Andrew Ng, and Honglak Lee. An Analysis of Single Layer Networks in Unsupervised Feature Learning. In *AISTATS*, 2011.

Zihang Dai, Hanxiao Liu, Quoc V. Le, and Mingxing Tan. Coatnet: Marrying convolution and attention for all data sizes. In *NeurIPS*, 2021.

Karan Desai and Justin Johnson. Virtex: Learning visual representations from textual annotations. In *CVPR*, 2021.

Jacob Devlin, Ming-Wei Chang, Kenton Lee, and Kristina Toutanova. Bert: Pre-training of deep bidirectional transformers for language understanding. In *NAACL*, 2018.

Alexey Dosovitskiy, Lucas Beyer, Alexander Kolesnikov, Dirk Weissenborn, Xiaohua Zhai, Thomas Unterthiner, Mostafa Dehghani, Matthias Minderer, Georg Heigold, Sylvain Gelly, Jakob Uszkoreit, and Neil Houlsby. An image is worth 16x16 words: Transformers for image recognition at scale. In *ICLR*, 2021.

M. Everingham, L. Van Gool, C. K. I. Williams, J. Winn, and A. Zisserman. The PASCAL Visual Object Classes Challenge 2007 (VOC2007) Results.

Fartash Faghri, David J Fleet, Jamie Ryan Kiros, and Sanja Fidler. Vse++: Improving visual-semantic embeddings with hard negatives. *BMVC*, 2017.

Li Fei-Fei, Fergus Rob, and Pietro Perona. Learning generative visual models from few training examples: An incremental bayesian approach tested on 101 object categories. In *CVPR*, 2004.

Andrea Frome, Greg Corrado, Jonathon Shlens, Samy Bengio, Jeffrey Dean, Marc’ Aurelio Ranzato, and Tomas Mikolov. Devise: A deep visual-semantic embedding model. In *Advances in Neural Information Processing Systems*, 2013.

Noah Golowich, Alexander Rakhlin, and Ohad Shamir. Size-independent sample complexity of neural networks. In *Conference On Learning Theory*, pages 297–299. PMLR, 2018.

Priya Goyal, Piotr Dollár, Ross B. Girshick, Pieter Noordhuis, Lukasz Wesolowski, Aapo Kyrola, Andrew Tulloch, Yangqing Jia, and Kaiming He. Accurate, large minibatch SGD: training imagenet in 1 hour. *Arxiv 1706.02677*, 2017.

- Andreas Griewank and Andrea Walther. Algorithm 799: revolve: an implementation of checkpointing for the reverse or adjoint mode of computational differentiation. *ACM Transactions on Mathematical Software (TOMS)*, 26(1):19–45, 2000.
- Kaiming He, Xiangyu Zhang, Shaoqing Ren, and Jian Sun. Deep residual learning for image recognition. In *CVPR*, 2015.
- Kaiming He, Haoqi Fan, Yuxin Wu, Saining Xie, and Ross B. Girshick. Momentum contrast for unsupervised visual representation learning. In *CVPR*, 2020.
- Patrick Helber, Benjamin Bischke, Andreas Dengel, and Damian Borth. Introducing eurosat: A novel dataset and deep learning benchmark for land use and land cover classification. In *IEEE International Geoscience and Remote Sensing Symposium*, 2018.
- Dan Hendrycks, Steven Basart, Norman Mu, Saurav Kadavath, Frank Wang, Evan Dorundo, Rahul Desai, Tyler Zhu, Samyak Parajuli, Mike Guo, Dawn Song, Jacob Steinhardt, and Justin Gilmer. The many faces of robustness: A critical analysis of out-of-distribution generalization. *ICCV*, 2021a.
- Dan Hendrycks, Kevin Zhao, Steven Basart, Jacob Steinhardt, and Dawn Song. Natural adversarial examples. *CVPR*, 2021b.
- Yasuhide Mori Hironobu, Hironobu Takahashi, and Ryuichi Oka. Image-to-word transformation based on dividing and vector quantizing images with words. In *Citeseer*, 1999.
- Micah Hodosh, Peter Young, and Julia Hockenmaier. Framing image description as a ranking task: Data, models and evaluation metrics. *Journal of Artificial Intelligence Research*, 2013.
- Jie Hu, Li Shen, and Gang Sun. Squeeze-and-excitation networks. In *Proceedings of the IEEE conference on computer vision and pattern recognition*, pages 7132–7141, 2018.
- Gao Huang, Yu Sun, Zhuang Liu, Daniel Sedra, and Kilian Weinberger. Deep networks with stochastic depth. In *BMVC*, 2017.
- Yanping Huang, Youlong Cheng, Ankur Bapna, Orhan Firat, Dehao Chen, Mia Chen, HyoukJoong Lee, Jiquan Ngiam, Quoc V Le, Yonghui Wu, et al. Gpipe: Efficient training of giant neural networks using pipeline parallelism. *Advances in neural information processing systems*, 32:103–112, 2019.
- Zhicheng Huang, Zhaoyang Zeng, Bei Liu, Dongmei Fu, and Jianlong Fu. Pixel-bert: Aligning image pixels with text by deep multi-modal transformers. *Arxiv 2004.00849*, 2020.
- Paras Jain, Ajay Jain, Aniruddha Nrusimha, Amir Gholami, Pieter Abbeel, Joseph Gonzalez, Kurt Keutzer, and Ion Stoica. Checkmate: Breaking the memory wall with optimal tensor rematerialization. *Proceedings of Machine Learning and Systems*, 2:497–511, 2020.
- Chao Jia, Yinfei Yang, Ye Xia, Yi-Ting Chen, Zarana Parekh, Hieu Pham, Quoc V. Le, Yunhsuan Sung, Zhen Li, and Tom Duerig. Scaling up visual and vision-language representation learning with noisy text supervision. In *ICML*, 2021.
- Armand Joulin, Laurens Van Der Maaten, Allan Jabri, and Nicolas Vasilache. Learning visual features from large weakly supervised data. In *ECCV*, 2016.
- Norman P. Jouppi, Cliff Young, Nishant Patil, David A. Patterson, Gaurav Agrawal, Raminder Bajwa, Sarah Bates, Suresh Bhatia, Nan Boden, Al Borchers, Rick Boyle, Pierre-luc Cantin, Clifford Chao, Chris Clark, Jeremy Coriell, Mike Daley, Matt Dau, Jeffrey Dean, Ben Gelb, Tara Vazir Ghaemmaghami, Rajendra Gottipati, William Gulland, Robert Hagmann, Richard C. Ho, Doug Hogberg, John Hu, Robert Hundt, Dan Hurt, Julian Ibarz, Aaron Jaffey, Alek Jaworski, Alexander Kaplan, Harshit Khaitan, Andy Koch, Naveen Kumar, Steve Lacy, James Laudon, James Law, Diemthu Le, Chris Leary, Zhuyuan Liu, Kyle Lucke, Alan Lundin, Gordon MacKean, Adriana Maggiore, Maire Mahony, Kieran Miller, Rahul Nagarajan, Ravi Narayanaswami, Ray Ni, Kathy Nix, Thomas Norrie, Mark Omernick, Narayana Penukonda, Andy Phelps, Jonathan Ross, Amir Salek, Emad Samadiani, Chris Severn, Gregory Sizikov, Matthew Snelham, Jed Souter, Dan Steinberg, Andy Swing, Mercedes Tan, Gregory Thorson, Bo Tian, Horia Toma, Erick Tuttle, Vijay . In-datacenter performance analysis of a tensor processing unit. *Arxiv 1704.04760*, 2017.
- Andrej Karpathy and Li Fei-Fei. Deep visual-semantic alignments for generating image descriptions. In *CVPR*, 2015.
- Diederik P. Kingma and Jimmy Ba. Adam: A method for stochastic optimization. In *ICLR*, 2015.
- Ryan Kiros, Ruslan Salakhutdinov, and Richard S Zemel. Unifying visual-semantic embeddings with multimodal neural language models. *Arxiv 1411.2539*, 2014.

- Alexander Kolesnikov, Lucas Beyer, Xiaohua Zhai, Joan Puigcerver, Jessica Yung, Sylvain Gelly, and Neil Houlsby. Big transfer (bit): General visual representation learning. In *ECCV*, 2020.
- Alex Krizhevsky. Learning multiple layers of features from tiny images. Technical report, 2009.
- Taku Kudo and John Richardson. Sentencepiece: A simple and language independent subword tokenizer and detokenizer for neural text processing. In *EMNLP*, 2018.
- Ravi Kumar, Manish Purohit, Zoya Svitkina, Erik Vee, and Joshua Wang. Efficient rematerialization for deep networks. *Advances in Neural Information Processing Systems*, 32, 2019.
- Hugo Larochelle, Dumitru Erhan, and Yoshua Bengio. Zero-data learning of new tasks. In *AAAI*, 2008.
- Yann LeCun, Corinna Cortes, and CJ Burges. Mnist handwritten digit database. *ATT Labs [Online]*. Available: <http://yann.lecun.com/exdb/mnist>, 2, 2010.
- Dmitry Lepikhin, HyukJoong Lee, Yuanzhong Xu, Dehao Chen, Orhan Firat, Yanping Huang, Maxim Krikun, Noam Shazeer, and Zhifeng Chen. Gshard: Scaling giant models with conditional computation and automatic sharding. *Arxiv 2006.16668*, 2020.
- Brian Lester, Rami Al-Rfou, and Noah Constant. The power of scale for parameter-efficient prompt tuning. In *EMNLP*, 2021.
- Ang Li, Allan Jabri, Armand Joulin, and Laurens van der Maaten. Learning visual n-grams from web data. In *ICCV*, 2017.
- Kunpeng Li, Yulun Zhang, Kai Li, Yuanyuan Li, and Yun Fu. Visual semantic reasoning for image-text matching. In *ICCV*, 2019.
- Fenglin Liu, Yuanxin Liu, Xuancheng Ren, Xiaodong He, and Xu Sun. Aligning visual regions and textual concepts for semantic-grounded image representations. *Arxiv 1905.06139*, 2019.
- Ilya Loshchilov and Frank Hutter. Decoupled weight decay regularization. In *ICLR*, 2019.
- Jiasen Lu, Dhruv Batra, Devi Parikh, and Stefan Lee. Vilbert: Pretraining task-agnostic visiolinguistic representations for vision-and-language tasks. *NeurIPS*, 2019.
- Dhruv Mahajan, Ross B. Girshick, Vignesh Ramanathan, Kaiming He, Manohar Paluri, Yixuan Li, Ashwin Bharambe, and Laurens van der Maaten. Exploring the limits of weakly supervised pretraining. In *ECCV*, 2018.
- Andreas Maurer. A vector-contraction inequality for rademacher complexities. In *International Conference on Algorithmic Learning Theory*, pages 3–17. Springer, 2016.
- Nicola Messina, Giuseppe Amato, Andrea Esuli, Fabrizio Falchi, Claudio Gennaro, and Stéphane Marchand-Maillet. Fine-grained visual textual alignment for cross-modal retrieval using transformer encoders. *ACM Transactions on Multimedia Computing, Communications, and Applications*, 2020.
- Mehryar Mohri, Afshin Rostamizadeh, and Ameet Talwalkar. *Foundations of machine learning*. MIT press, 2012.
- Hyeonseob Nam, Jung-Woo Ha, and Jeonghee Kim. Dual attention networks for multimodal reasoning and matching. In *CVPR*, 2017.
- Yurii E. Nesterov. A method for solving the convex programming problem with convergence rate $o(1/k^2)$. *Soviet Mathematics Doklady*, 1983.
- Maria-Elena Nilsback and Andrew Zisserman. Automated flower classification over a large number of classes. In *Indian Conference on Computer Vision, Graphics and Image Processing*, 2008.
- Mohammad Norouzi, Tomas Mikolov, Samy Bengio, Yoram Singer, Jonathon Shlens, Andrea Frome, Greg S Corrado, and Jeffrey Dean. Zero-shot learning by convex combination of semantic embeddings. *Arxiv 1312.5650*, 2013.
- Myle Ott, Sergey Edunov, David Grangier, and Michael Auli. Scaling neural machine translation. In *Workshop in Neural Machine Translation*, 2018.
- Omkar M Parkhi, Andrea Vedaldi, Andrew Zisserman, and CV Jawahar. Cats and dogs. *CVPR*, 2012.
- Hieu Pham, Zihang Dai, Qizhe Xie, Minh-Thang Luong, and Quoc V. Le. Meta pseudo labels. In *CVPR*, 2021.
- Alec Radford, Jong Wook Kim, Chris Hallacy, Aditya Ramesh, Gabriel Goh, Sandhini Agarwal, Girish Sastry, Amanda Askell, Pamela Mishkin, Jack Clark, Gretchen Krueger, and Ilya Sutskever. Learning transferable visual models from natural language supervision. In *ICML*, 2021.
- Benjamin Recht, Rebecca Roelofs, Ludwig Schmidt, and Vaishaal Shankar. Do imagenet classifiers generalize to imagenet? In *ICML*, 2019.
- Olga Russakovsky, Jia Deng, Hao Su, Jonathan Krause, Sanjeev Satheesh, Sean Ma, Zhiheng Huang, Andrej Karpathy, Aditya Khosla, Michael Bernstein, Alexander C. Berg, and Li Fei-Fei. ImageNet Large Scale Visual Recognition

- Challenge. *IJCV*, 2009.
- Mert Bulent Sariyildiz, Julien Perez, and Diane Larlus. Learning visual representations with caption annotations. In *ECCV*, 2020.
- Edgar Schönfeld, Sayna Ebrahimi, Samarth Sinha, Trevor Darrell, and Zeynep Akata. Generalized zero- and few-shot learning via aligned variational autoencoders. In *CVPR*, 2019.
- Shai Shalev-Shwartz and Shai Ben-David. *Understanding machine learning: From theory to algorithms*. Cambridge university press, 2014.
- Noam Shazeer and Mitchell Stern. Adafactor: Adaptive learning rates with sublinear memory cost. *Arxiv 1804.04235*, 2018.
- Noam Shazeer, Youlong Cheng, Niki Parmar, Dustin Tran, Ashish Vaswani, Penporn Koanantakool, Peter Hawkins, HyukJoong Lee, Mingsheng Hong, Cliff Young, et al. Mesh-tensorflow: Deep learning for supercomputers. *Arxiv 1811.02084*, 2018.
- Richard Socher and Li Fei-Fei. Connecting modalities: Semi-supervised segmentation and annotation of images using unaligned text corpora. In *CVPR*, 2010.
- Richard Socher, Milind Ganjoo, Hamsa Sridhar, Osbert Bastani, Christopher D Manning, and Andrew Y Ng. Zero-shot learning through cross-modal transfer. In *Advances in Neural Information Processing Systems*, 2013.
- Richard Socher, Andrej Karpathy, Quoc V. Le, Christopher D. Manning, and Andrew Y. Ng. Grounded compositional semantics for finding and describing images with sentences. *TACL*, 2014.
- Khurram Soomro, Amir Roshan Zamir, and Mubarak Shah. UCF101: A dataset of 101 human actions classes from videos in the wild. *Arxiv 1212.0402*, 2012.
- Nitish Srivastava, Geoffrey Hinton, Alex Krizhevsky, Ilya Sutskever, and Ruslan Salakhutdinov. Dropout: A simple way to prevent neural networks from overfitting. In *JMLR*, 2014.
- Chen Sun, Abhinav Shrivastava, Saurabh Singh, and Abhinav Gupta. Revisiting unreasonable effectiveness of data in deep learning era. In *ICCV*, 2017.
- Christian Szegedy, Wojciech Zaremba, Ilya Sutskever, Joan Bruna, Dumitru Erhan, Ian Goodfellow, and Rob Fergus. Intriguing properties of neural networks. *Arxiv 1312.6199*, 2013.
- Mingxing Tan and Quoc V. Le. Efficientnet: Rethinking model scaling for convolutional neural networks. In *ICML*, 2019.
- Mingxing Tan and Quoc V. Le. Efficientnetv2: Smaller models and faster training. In *ICML*, 2021.
- Mingxing Tan, Ruoming Pang, and Quoc V. Le. Efficientdet: Scalable and efficient object detection. In *CVPR*, 2020.
- Rohan Taori, Achal Dave, Vaishaal Shankar, Nicholas Carlini, Benjamin Recht, and Ludwig Schmidt. Measuring robustness to natural distribution shifts in image classification. In *NeurIPS*, 2020.
- Yonglong Tian, Chen Sun, Ben Poole, Dilip Krishnan, Cordelia Schmid, and Phillip Isola. What makes for good views for contrastive learning? In *NeurIPS*, 2020.
- Tijmen Tieleman and Geoffrey Hinton. RmsProp: Divide the gradient by a running average of its recent magnitude. COURSERA: Neural Networks for Machine Learning, 2012.
- Hugo Touvron, Andrea Vedaldi, Matthijs Douze, and Hervé Jégou. Fixing the train-test resolution discrepancy. In *NeurIPS*, 2019.
- Aäron van den Oord, Yazhe Li, and Oriol Vinyals. Representation learning with contrastive predictive coding. *Arxiv 1807.03748*, 2018.
- Ashish Vaswani, Noam Shazeer, Niki Parmar, Jakob Uszkoreit, Llion Jones, Aidan N Gomez, Łukasz Kaiser, and Illia Polosukhin. Attention is all you need. In *Advances in neural information processing systems*, 2017.
- Bastiaan S Veeling, Jasper Linmans, Jim Winkens, Taco Cohen, and Max Welling. Rotation equivariant CNNs for digital pathology. *Medical Image Computing and Computer Assisted Intervention*, 2018.
- Oriol Vinyals, Alexander Toshev, Samy Bengio, and Dumitru Erhan. Show and tell: A neural image caption generator. In *CVPR*, 2015.
- Haohan Wang, Songwei Ge, Zachary Lipton, and Eric P Xing. Learning robust global representations by penalizing local predictive power. In *NeurIPS*, 2019.
- Zhou Wang, Alan C Bovik, Hamid R Sheikh, and Eero P Simoncelli. Image quality assessment: from error visibility to structural similarity. *IEEE transactions on image processing*, 13(4):600–612, 2004.

- Jason Weston, Samy Bengio, and Nicolas Usunier. Large scale image annotation: learning to rank with joint word-image embeddings. *Machine Learning*, 2010.
- Yongqin Xian, Zeynep Akata, Gaurav Sharma, Quynh N. Nguyen, Matthias Hein, and Bernt Schiele. Latent embeddings for zero-shot classification. In *CVPR*, 2016.
- Yongqin Xian, Bernt Schiele, and Zeynep Akata. Zero-shot learning - the good, the bad and the ugly. In *CVPR*, 2017.
- Jianxiong Xiao, James Hays, Krista A. Ehinger, Aude Oliva, and Antonio Torralba. Sun database: Large-scale scene recognition from abbey to zoo. In *CVPR*, 2010.
- Qizhe Xie, Minh-Thang Luong, Eduard Hovy, and Quoc V Le. Self-training with noisy student improves imagenet classification. In *CVPR*, 2020.
- Kelvin Xu, Jimmy Ba, Ryan Kiros, Kyunghyun Cho, Aaron Courville, Ruslan Salakhudinov, Rich Zemel, and Yoshua Bengio. Show, attend and tell: Neural image caption generation with visual attention. In *ICML*, 2015.
- Yuanzhong Xu, HyounJoong Lee, Dehao Chen, Blake Hechtman, Yanping Huang, Rahul Joshi, Maxim Krikun, Dmitry Lepikhin, Andy Ly, Marcello Maggioni, et al. Gspmd: General and scalable parallelization for ml computation graphs. *arXiv preprint arXiv:2105.04663*, 2021.
- Li Yuan, Qibin Hou, Zihang Jiang, Jiashi Feng, and Shuicheng Yan. Volo: Vision outlooker for visual recognition. *ArXiv 2106.13112*, 2021.
- Xiaohua Zhai, Alexander Kolesnikov, Neil Houlsby, and Lucas Beyer. Scaling vision transformers. In *Arxiv 2106.04560*, 2021.
- Xiaohua Zhai, Xiao Wang, Basil Mustafa, Andreas Steiner, Daniel Keysers, Alexander Kolesnikov, and Lucas Beyer. Lit: Zero-shot transfer with locked-image text tuning. In *Proceedings of the IEEE/CVF Conference on Computer Vision and Pattern Recognition*, pages 18123–18133, 2022.
- Li Zhang, Tao Xiang, and Shaogang Gong. Learning a deep embedding model for zero-shot learning. In *CVPR*, 2017.
- Yuhao Zhang, Hang Jiang, Yasuhide Miura, Christopher D Manning, and Curtis P Langlotz. Contrastive learning of medical visual representations from paired images and text. *Arxiv 2010.00747*, 2020.

A. Model sizes

In our preliminary experiments, we experimented with different model sizes. Table 5 presents the final, most compute-to-performance efficient model sizes, which we use throughout the paper.

	Image model			Text model				
	Model (Dai et al., 2021)	#Params	#FLOPs	#Layers	HiddenDim	HeadDim	#Params	#FLOPs
BASIC-S	CoAtNet-0	25M	4.2B	6	1024	64	108M	10.7B
BASIC-M	CoAtNet-3	168M	34.7B	12	1024	128	184M	49.4B
BASIC-L	CoAtNet-7	2.4B	495.8B	12	2048	128	670M	212.6B

Table 5: Model sizes. For the image models, all specifications can be found from the model names in Dai et al. (2021).

B. Hyperparameters and other implementation details

Our training and evaluation code will eventually be released. Here, we summarize a few important details. All of our hyper-parameters are in Table 6.

No regularization. Other than the decoupled weight decay in AdaFactorW, we do not use any other regularization technique. In fact, we find that with BASIC-S and BASIC-M, if we add other forms of regularization such as stochastic depth (Huang et al., 2017) or dropout (Srivastava et al., 2014), our ImageNet top-1 accuracy drops substantially. This suggests that our datasets are very large and perhaps in such situation, regularization techniques do more harm than good by causing optimization difficulty to our models.

Another important effect of *not* using regularization in our training framework is to make the re-materialization steps in Section 4.2 consistent. If we apply random perturbations to our forward passes, *e.g.* by skipping layers like in stochastic depth or by setting random values to zeros, then two forward passes for re-materialization (see Lines 2-5 and 11-14 in Algorithm 1) will compute two different passes. While we could treat such difference as a form of regularization noise, our early experiment show that with dropout-like regularizations, our training loss stays relatively large throughout the course of training. This observation suggests that the noise causes some optimization difficulty to our models, so we opt not to use any dropout-like regularization.

	BASIC-S		BASIC-{M,L}	
	Pretraining	Contrastive	Pretraining	Contrastive
Optimizer	AdaFactorW	AdaFactorW	AdaFactorW	AdaFactorW
Batch size	16384	65536	16384	65536
Training steps	500K	500K	1.2M	500K
Warm-up steps	25K	25K	25K	25K
Max learning rate	1e-3	1e-3	4e-4	2.5e-4
Min learning rate	1e-5	1e-5	2e-5	1e-5
Learning decay schedule	Cosine	Cosine	Linear	Cosine
Weight decay	0.005	0.0025	0.01	0.0025

Table 6: Hyperparameters all of our experiments.

C. Evaluation Datasets Details

Here, we present the details of the datasets which we use to evaluate our BASIC models in Section 9.2. It is worth noting that *not* all these datasets use the accuracy as the performance metric. This is because these datasets have a certain level of imbalance between their classes, as well as other properties that make them accuracy not the best suitable metric for them. For instance, the dataset Caltech-101 has a class called “Background” which refers to *any* image that does not belong to its predefined 101 classes. One certainly cannot come up with a textual description that describes this “class”. As such, Caltech-101 is evaluated using mean per-class recall. Details about other datasets are in Table 7.

Dataset	Reference	Abbreviation in Table 3	#Classes	Test size	Evaluation metric
ILSVRC-2012, <i>i.e.</i> , ImageNet	(Russakovsky et al., 2009)	ImageNet	1000	50000	accuracy
ImageNet-A	(Hendrycks et al., 2021b)	N/A	1000	7500	accuracy
ImageNet-R	(Hendrycks et al., 2021a)	N/A	1000	30000	accuracy
ImageNet-V2	(Recht et al., 2019)	N/A	1000	10000	accuracy
ImageNet-Sketch	(Wang et al., 2019)	N/A	1000	50889	accuracy
ObjectNet	(Barbu et al., 2019)	N/A	1000	18574	accuracy
CIFAR-10	(Krizhevsky, 2009)	CIFAR10	10	10000	accuracy
CIFAR-100	(Krizhevsky, 2009)	CIFAR100	100	10000	accuracy
Birdsnap	(Berg et al., 2014)	Birdsnap	500	2443	accuracy
Describable Textures	(Cimpoi et al., 2014)	DTD	47	1880	accuracy
Oxford Flowers-102	(Nilsback and Zisserman, 2008)	Flowers	102	6149	mean per-class recall
Food-101	(Bossard et al., 2014)	Food101	101	25250	accuracy
Caltech101	(Fei-Fei et al., 2004)	Caltech101	102	6084	mean per-class recall
Oxford IIIT-Pets	(Parkhi et al., 2012)	IIIT-Pets	37	3669	mean per-class recall
MNIST	(LeCun et al., 2010)	MNIST	10	10000	accuracy
EuroSAT	(Helber et al., 2018)	EuroSAT	10	27000	accuracy
PatchCamelyon	(Veeling et al., 2018)	PCam	2	32768	accuracy
RESICS45	(Cheng et al., 2017)	RESICS45	45	31500	accuracy
STL10	(Coates et al., 2011)	STL10	10	8000	accuracy
SUN397	(Xiao et al., 2010)	SUN397	397	21750	accuracy
UCF101	(Soomro et al., 2012)	UCF101	101	3783	accuracy
Pascal VOC 2007 Classification	(Everingham et al.)	VOC2007	20	4952	11-points mAP

Table 7: Details of the datasets used in this paper to evaluate BASIC models. The evaluation results are presented in Table 1 and Table 3.

D. Further Discussion on Robustness

In Section 9.3, we present a surprising result: finetuning converged BASIC checkpoints on *more* ImageNet labeled data leads to *worse* robustness results. The metric for robustness in Section 9.3 is the *average* top-1 accuracy of the finetuned models on 5 robustness benchmarks derived from ImageNet (Hendrycks et al., 2021b,a; Recht et al., 2019; Barbu et al., 2019; Wang et al., 2019). It turns out that each of these benchmarks can demonstrate slightly different results for the finetuned models. Here, we discuss such benchmarks.

ImageNet-V2 (Recht et al., 2019). This dataset is collected in a process that closely follows the process to collect and annotate the images in the standard ILSVRC-2012 validation set, which is typically referred to as “ImageNet” in the literature (and our paper as well). As such, gains observed on ImageNet often transfer to ImageNet-V2. Recent works such as EfficientNets (Tan and Le, 2019, 2021) or ViT (Dosovitskiy et al., 2021) also demonstrate the similar trend. For our experiment in Section 9.3, BASIC-M’s robustness accuracy improves along with its ImageNet accuracy, following this trend. However, BASIC-L’s robustness does not.

We suspect this trend is because BASIC-L’s learning capacity is larger than that of BASIC-M, so BASIC-L picks up more “spurious” patterns from ImageNet, making it less robust than BASIC-M.

ImageNet-R (Wang et al., 2019). ImageNet-R is a special robustness dataset in our study. Not only of our BASIC models but also other zero-shot models – CLIP and ALIGN – are more accurate on ImageNet-R than they are on ImageNet (see Table 1). These data points alone would suggest that ImageNet-R is somewhat easier than ImageNet, until we look at the significant accuracy drops for other methods on ImageNet-R. For instance, Noisy Student (Xie et al., 2020) and Meta Pseudo Labels (Pham et al., 2021) respectively achieve only 74.9% and 72.7% accuracy on ImageNet-R, despite their accuracy of 88.4% and 90.2% on ImageNet ILSVRC-2012. The real reason for such discrepancy in ImageNet-R is that ImageNet-R is collected by selecting the ImageNet classes from visual art pieces, such as paintings, cartoons, graffiti, origami, and sculptures. These art pieces are often displayed in a clean environment, free of noises such as multiple classes per image, making the images easier to recognize. As such, BASIC, CLIP, and ALIGN, all perform better on ImageNet-R. However, ImageNet-R images have a drastically different distribution compared to ImageNet *labeled* training images, as they are respectively art images and natural images. This is why ImageNet-trained models display a much lower accuracy on ImageNet, compared to zero-shot models.

The case of ObjectNet (Barbu et al., 2019). From Table 1, it can be seen that BASIC model’s improvement over ALIGN and CLIP on Object is significantly lower than others on other benchmarks, *i.e.*, 6.6% compared to more than 8% (except for ImageNet-R, for which the accuracy of all models are saturated at over 90%). We find out the reason is that, even though ObjectNet has images from the same classes with ImageNet, these objects turn out to have their own more descriptive names, *e.g.* the class name “chairs” in ImageNet could be “chairs by [viewpoint]” or “chairs with [background]”. As we later show in Section G, using different class names and prompts can affect our results. This effect has also been observed in CLIP (Radford et al., 2021). Here, we take the same class names and prompts for ImageNet and use them for ObjectNet. We suspect that using ObjectNet-specific class names and prompts can improve our result.

E. Computational Cost

All of our models are implemented in TensorFlow (Abadi et al., 2016) and trained on Tensor Processing Units (TPUs (Jouppi et al., 2017)). Our BASIC-S and BASIC-M models are all trained on TPUv3 chips, while our BASIC-L models are trained on TPUv4 chips. These TPUv4 chips in their MegaCore mode can offer 32GB of memory, out of which our BASIC-L models use 30.1GB, which means that our model essentially saturates the TPU’s memory. We note that oftentimes, a small portion of TPU memory needs to be reserved for their low-level infra systems. Therefore, our BASIC-L models essentially saturate the accelerators with the largest memory currently available. Given this memory usage, we use Algorithm 1 with the microbatch size $M = 8192$ and the batch size $N = 65536$ to train this model. Table 8 summarizes the training cost for each phase of our models BASIC- $\{S,M,L\}$ as in Section 9.2.

F. Qualitative Analysis: Successful Classification Examples

Zero-shot transfer models open the door to versatile applications. This section is dedicated to demonstrating their versatility. In Figure 7, we visualize some predictions of our best model, BASIC-L, on instances that are less expected on traditional image classification benchmarks. We come up with the text sequences and demonstrate that the model can indeed align images to the most appropriate sequence.

Model	Pretraining		Text Encoder		Text & Image Encoders	
	Type	Cores×Days	Type	Cores×Days	Type	Cores×Days
BASIC-S	TPUv3	0.4K	TPUv3	0.9K	TPUv3	0.3K
BASIC-M	TPUv3	1.7K	TPUv3	3.9K	TPUv3	1.2K
BASIC-L	TPUv4	6.9K	TPUv4	1.0K	TPUv4	0.8K

Table 8: Computational usages to train our models. Core×Days is the product of the number of training days and the number of cores used to train the models. For instance, using 2048 TPUs in 1 day equals to 2.048 Cores×Days. We use this metric because sometimes, our jobs are run on different numbers of TPUs due to limited availability.





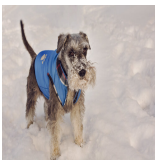

	<i>Eggs with mixed expressions.</i> (✓) <i>Emojis with mixed expressions.</i> <i>Happy eggs.</i> <i>Sad eggs.</i> <i>Happy emojis.</i> <i>Sad emojis.</i>	0.944 0.032 0.022 0.002 <1e-3 <1e-3		<i>One plus one equals three.</i> (✓) <i>One plus one equals one.</i> <i>One plus one equals two.</i> <i>One minus one equals three.</i> <i>One minus one equals two.</i> <i>One minus one equals one.</i> <i>Chemistry equation on a whiteboard.</i> (✓)	0.468 0.264 0.240 0.014 <1e-3 <1e-3 0.958
	<i>Cosplayed pikachu.</i> (✓) <i>Cosplayed charmander.</i> <i>Real pikachu.</i> <i>Cosplayed eevee.</i> <i>Real charmander.</i> <i>Real eevee.</i>	0.764 0.219 0.012 0.006 <1e-3 <1e-3		<i>Math equation on a whiteboard.</i> <i>Physics equation on a whiteboard.</i> <i>Chemistry equation on a paper.</i> <i>Math equation on a paper.</i> <i>Physics equation on a paper.</i> <i>An alarm clock that reads 7:00 pm.</i> (✓)	0.024 0.012 0.005 <1e-3 <1e-3 0.288
	<i>A shirari dog in cold weather.</i> (✓) <i>A shirari dog in warm weather.</i> <i>A corgi dog in cold weather.</i> <i>A shiba inu dog in cold weather.</i> <i>A corgi dog in warm weather.</i> <i>A shiba inu dog in warm weather.</i>	0.961 0.038 <1e-3 <1e-3 <1e-3 <1e-3		<i>An alarm clock that reads 10:00 am.</i> <i>An alarm clock that reads 12:00 pm.</i> <i>An alarm clock that reads 4:00 pm.</i> <i>An alarm clock that reads 7:00 am.</i> <i>An alarm clock that reads 2:00 pm.</i>	0.183 0.167 0.162 0.133 0.067

Figure 7: Selected classification examples from BASIC-L over unseen images.

G. Failure Analysis

Most machine learning models fail in certain tests. It is important to identify such failure cases, to understand the failing causes, and if possible, to come up with fixes. Here, we first look at the test benchmarks in Table 3 from Section 9.2 where BASIC models perform worse than CLIP models. We identify the cause of failures for BASIC models and recommend certain fixes that can improve their performance. Then, in Section G.2, we present some erroneous behaviors of BASIC models via selected examples. These examples reveal some weaknesses of zero-shot transfer models, and invite future research to improve them.

G.1 The benchmarks where BASIC fails

From Section 9.2, we see that BASIC models have particularly low performance on EuroSat (Helber et al., 2018), MNIST (LeCun et al., 2010), and Patch Camelyon (Veeling et al., 2018). The accuracy of BASIC-L on these datasets are 51.0%, 40.3%, and 59.6% respectively. For what it’s worth, BASIC-L’s accuracy are better than those of our smaller models, *i.e.*, BASIC-S and BASIC-M, so our central message in this paper – scaling helps – is not altered. Here, we focus on analyzing the failures of BASIC-L.

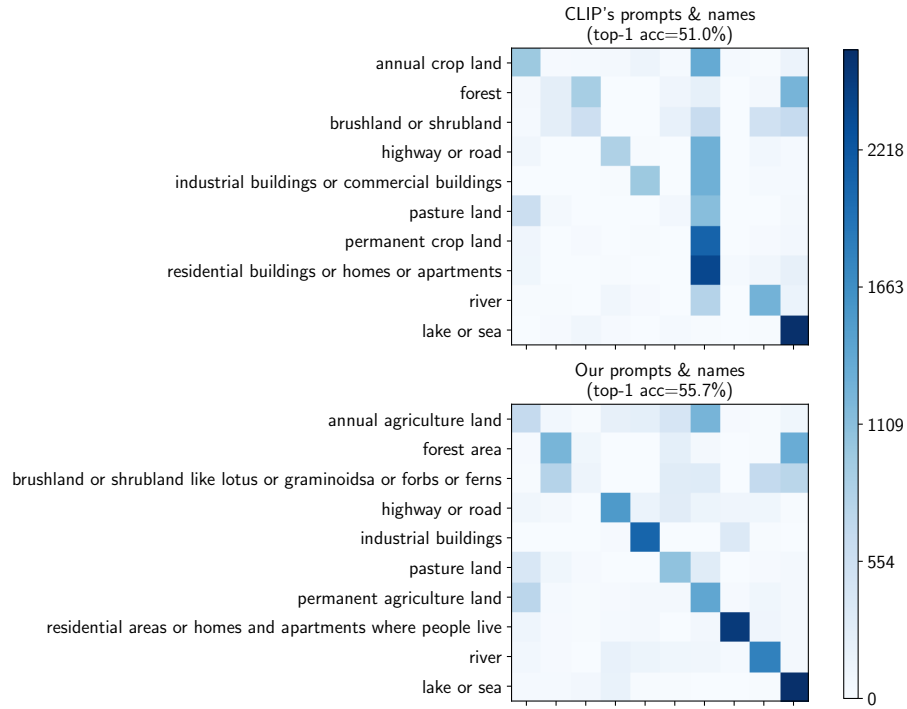
Patch Camelyon (PCam). PCam is perhaps the most sensitive dataset among the three benchmarks where BASIC-L performs poorly. This dataset consists of images extracted from histopathologic scans of lymph node sections, and models are asked to make the binary prediction – whether an input image has a cancerous lymph node or not. For such an important task, the top-1 accuracy of both BASIC-L (59.6%) and CLIP (63.0%) are far below the bars for practical deployments. We remark that PCam is a binary classification task, so the accuracy of BASIC-L and CLIP are just slightly above random guessing. Their poor performance, however, are quite understandable: classifying lymph nodes requires much more specific training, compared to classifying common natural images. As our training data are weakly crawled and automatically curated from the internet, without any emphasis on medical images, our BASIC-L model cannot learn enough to perform well on PCam. We suspect the same speculation also holds for CLIP, as their data collection and curation process is comparable to ours. Finally, the low accuracy of CLIP and BASIC models on PCam is an assertion that despite the benefits of zero-shot transfer models, they are not ready to be deployed to tasks that require in-domain expertise, *e.g.* medical knowledge.

EuroSAT. This dataset consists of satellite images taken for certain types of lands. Models are asked to classify input images into one out of 10 given types of lands. The land types can be seen in Figure 8. The failure of BASIC-L on EuroSAT is an example for the importance of prompt engineering in zero-shot transfer learning for image-text models. In Figure 8, we show that by changing the dataset’s *class names* and the model’s set of prompts, into words and phrases that essentially have the same meaning to humans, we can improve the accuracy of BASIC-L from 51.0% to 55.7%. We do not further explore the changes in class names and prompts to improve BASIC-L’s performance on EuroSAT, as they belong to a different topic from the focus of this paper – combined scaling. However, our findings on this EuroSAT dataset suggests that contrastive image-text models do not really “understand” texts. This is perhaps because of the low quality of the texts in our training data, unlike the millions of words from books and articles like the training data of NLP models such as BERT (Devlin et al., 2018).

MNIST. MNIST is a classical dataset in computer vision for handwritten digit classification. Simple models can achieve more than 99.5% accuracy, and yet BASIC-L achieves the humble 40.3% accuracy. Unlike the case of PCam, *i.e.* there is not enough training data in our training dataset, for MNIST, we find that the ALIGN dataset has a fair amount of images that contain digits, either handwritten or printed. This means that the image encoder of BASIC-L has seen digit figures, and suggests that the failures might be more attributable to the text encoder, similar to the case of EuroSAT. In Figure 9, we show the confusion matrices of BASIC-L models with three sets of class names: using the digits such as {‘0’, ‘1’, ...}, using the texts such as {‘one’, ‘two’, ...}, and using both such as {‘0 or zero’, ‘1 or one’, ...}. Unfortunately, we cannot improve BASIC-L’s accuracy on MNIST, like we did for EuroSAT: BASIC-L’s accuracy is low in all three cases, but the confusion matrices are visibly different: BASIC-L models ‘thinks’ that many digits look like ‘3’ for the digit-only class names, but many digits look like ‘1 or one’ in the digit-and-text class names. Again, humans who understand languages will not make these mistakes. We think these mistakes constitute a new type or robustness failures, which we hope will invite further research.

G.2 Example failure cases

From the confusion matrices of BASIC-L on two benchmarks, EuroSAT (Helber et al., 2018) and MNIST (LeCun et al., 2010), we observe that the prompts and class names are crucial for the performance of zero-shot transfer models. Here, we select and present a few examples to demonstrate the failures of BASIC-L. Figure 10 visualizes these examples.



Prompts from CLIP (Radford et al., 2021)	Prompts we find
'a centered satellite photo of {}.'	'a centered satellite photo of {}'
'a centered satellite photo of a {}.'	'a satellite photo of {}'
'a centered satellite photo of the {}.'	'a photo of {} taken from a satellite'
	'a photo of {} taken from the sky'
	'a picture of {} taken from the sky by a satellite'
	'a picture of {} taken by a satellite'
	'a picture of {} taken by a satellite in space'
	'a picture of {} taken by a satellite in its orbit'

Figure 8: Confusion matrices of BASIC-L on the EuroSAT classification dataset (Helber et al., 2018). Shown are the confusion matrices obtained from zero-shot transfer learning from BASIC-L, using prompts and class names and CLIP, compared to the same model using prompts and class names that we tuned. The zero-shot top-1 accuracy with our prompts and class names are 4.7% higher, and the confusion matrix illustrates this by showing more concentration on the diagonal.

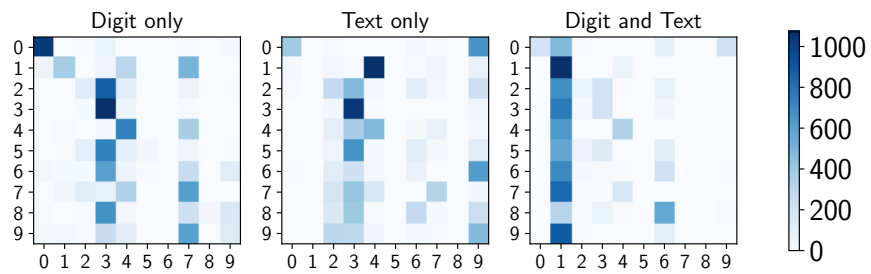


Figure 9: Confusion matrices of BASIC-L’s predictions on MNIST. **Digit only:** we use the class names {“0”, “1”, ..., “9”}; **Text only:** {“one”, “two”, ..., “nine”}; **Digit and Text:** {“0 or zero”, “1 or one”, ..., “9 or nine”}. The model has vastly different confusion matrices for different class name, suggesting that it does not understand the meaning of these strings, but instead, simply learns to match their embeddings.








	<i>More than 6 kittens in total.</i> (✗)	0.472		<i>No strawberries found in the photo.</i> (✗)	0.393
	<i>More than 4 kittens in total.</i>	0.342		<i>No blueberries found in the photo.</i>	0.304
	<i>More than 2 kittens in total.</i>	0.186		<i>No bananas found in the photo.</i>	0.297
	<i>More than 6 puppies in total.</i>	<1e-3		<i>No coconuts found in the photo.</i>	0.003
	<i>More than 2 puppies in total.</i>	<1e-3		<i>No pineapples found in the photo.</i>	0.002
	<i>More than 4 puppies in total.</i>	<1e-3		<i>No oranges found in the photo.</i>	0.001
	<i>Closed road.</i> (✗)	0.716		<i>Traffic sign indicating intersection.</i> (✓)	0.927
	<i>Slippery road.</i>	0.170		<i>Traffic sign indicating closed road.</i>	0.027
	<i>Intersection.</i>	0.076		<i>Traffic sign indicating sharp left.</i>	0.027
	<i>Stop.</i>	0.034		<i>Traffic sign indicating sharp right.</i>	0.016
	<i>Sharp left.</i>	0.003		<i>Traffic sign indicating slippery road.</i>	0.003
	<i>Sharp right.</i>	0.002		<i>Traffic sign indicating stop.</i>	<1e-3
	<i>red light saber.</i> (✓)	0.992		<i>blue light saber.</i> (✓)	0.990
	<i>blue light saber.</i>	0.005		<i>red light saber.</i>	0.004
	<i>red led light.</i>	0.002		<i>blue led light.</i>	0.003
	<i>red neon light.</i>	<1e-3		<i>blue neon light.</i>	0.003
	<i>blue led light.</i>	<1e-3		<i>red led light.</i>	<1e-3
	<i>blue neon light.</i>	<1e-3		<i>red neon light.</i>	<1e-3
	<i>a blue light saber on the left and a red light saber on the right.</i> (✗)	0.297			
	<i>a blue light saber on the right and a red light saber on the left.</i>	0.235			
	<i>a red light saber on the left and a blue light saber on the right.</i>	0.205			
	<i>a red light saber on the right and a blue light saber on the left.</i>	0.173			
	<i>a red light saber to the right of a blue light saber.</i>	0.054			
	<i>a red light saber to the left of a blue light saber.</i>	0.0342			

Figure 10: Selected failure cases for BASIC-L over unseen images. **(1)** The first block indicates that the model is not precise in object counting and does not well handle negation in the prompts, possibly due the nature of our training data. **(2)** The middle block shows two examples to indicate that prompt engineering can play a critical role in providing the model with sufficient context to produce the desired output. **(3)** The last block shows that the model does not have the sense of left and right, which is a relic of random left-right flips of images which we apply during training.

H. Proofs

In this appendix, we complete the proof of Theorem 1 and Theorem 2 by gradually analyzing the gap from the general case to the special case.

H.1 General case

Lemma 3 *Let \mathcal{F} be a set of maps $x \mapsto F(x)$ and \mathcal{G} be a set of maps $y \mapsto G(y)$. Then, for any $\delta > 0$, with probability at least $1 - \delta$, the following holds for all $F \in \mathcal{F}$ and $G \in \mathcal{G}$:*

$$\begin{aligned}
& \mathbb{E}_{x,y}[\bar{\ell}_M(x,y)] - \hat{\mathbb{E}}_S[\hat{\ell}_B(x,y)] \\
& \leq c_1 \mathbb{E}_{x,y}[A(x,y)] \left(\frac{1}{\sqrt{2B}} \left(2\sqrt{2}c_8c_9 + c_1\sqrt{\kappa \ln(\sqrt{\kappa B}/\delta)} \right) + \frac{2}{c_1} \sup_{x \in \mathcal{X}} \mathcal{R}_B(\mathcal{H}_{\mathcal{F},\mathcal{G},e}^x) \right) \\
& \quad + 2\mathcal{R}_m(\mathcal{H}_{\mathcal{F},\mathcal{G},\hat{\ell}_B}) + c_2 \sqrt{\frac{\ln(2/\delta)}{2m}}.
\end{aligned} \tag{5}$$

where $\mathcal{H}_{\mathcal{F},\mathcal{G},e}^x = \{y \mapsto \exp(F(x)^\top G(y)) : F \in \mathcal{F}, G \in \mathcal{G}\}$, $\mathcal{H}_{\mathcal{F},\mathcal{G},\hat{\ell}_B} = \{(x, y) \mapsto \hat{\ell}_B(x, y) : F \in \mathcal{F}, G \in \mathcal{G}\}$, and

$$A(x, y) = \frac{\exp(F(x)^\top G(y))}{\left(\frac{1}{B} \sum_{k=1}^B \exp(F(x)^\top G(\hat{y}_k))\right) \mathbb{E}_{\bar{y}}[\exp(F(x)^\top G(\bar{y}))]}.$$

Here, $\mathcal{R}_m(\mathcal{H}) := \mathbb{E}_{S,\sigma}[\sup_{h \in \mathcal{H}} \frac{1}{m} \sum_{i=1}^m \sigma_i h(x_i, y_i)]$ where $\sigma_1, \dots, \sigma_m$ are independent uniform random variables taking values in $\{-1, 1\}$.

Proof We first decompose the difference as follows:

$$\mathbb{E}_{x,y}[\bar{\ell}_M(x, y)] - \hat{\mathbb{E}}_S[\hat{\ell}_B(x, y)] = \mathbb{E}_{x,y}[\bar{\ell}_M(x, y)] - \mathbb{E}_{x,y}[\hat{\ell}_B(x, y)] + \mathbb{E}_{x,y}[\hat{\ell}_B(x, y)] - \hat{\mathbb{E}}_S[\hat{\ell}_B(x, y)] \quad (6)$$

$$= \mathbb{E}_{x,y}[\bar{\ell}_M(x, y) - \hat{\ell}_B(x, y)] + (\mathbb{E}_{x,y}[\hat{\ell}_B(x, y)] - \hat{\mathbb{E}}_S[\hat{\ell}_B(x, y)]). \quad (7)$$

For the inside of the expectation in the first term, we can write it as

$$\bar{\ell}_M(x, y) - \hat{\ell}_B(x, y) \quad (8)$$

$$= \frac{\exp(F(x)^\top G(y))}{\frac{1}{B} \sum_{k=1}^B \exp(F(x)^\top G(\hat{y}_k))} - \frac{\exp(F(x)^\top G(y))}{\mathbb{E}_{\bar{y}}[\exp(F(x)^\top G(\bar{y}))]} \quad (9)$$

$$= \frac{\exp(F(x)^\top G(y)) \mathbb{E}_{\bar{y}}[\exp(F(x)^\top G(\bar{y}))] - \exp(F(x)^\top G(y)) \left(\frac{1}{B} \sum_{k=1}^B \exp(F(x)^\top G(\hat{y}_k))\right)}{\left(\frac{1}{B} \sum_{k=1}^B \exp(F(x)^\top G(\hat{y}_k))\right) \mathbb{E}_{\bar{y}}[\exp(F(x)^\top G(\bar{y}))]} \quad (10)$$

$$= \frac{\exp(F(x)^\top G(y)) \left(\mathbb{E}_{\bar{y}}[\exp(F(x)^\top G(\bar{y}))] - \frac{1}{B} \sum_{k=1}^B \exp(F(x)^\top G(\hat{y}_k))\right)}{\left(\frac{1}{B} \sum_{k=1}^B \exp(F(x)^\top G(\hat{y}_k))\right) \mathbb{E}_{\bar{y}}[\exp(F(x)^\top G(\bar{y}))]} \quad (11)$$

Using Lemma 4 (see below) with the assumption that $\hat{y}_1, \hat{y}_2, \dots, \hat{y}_B \stackrel{iid}{\sim} p_y$ and $\exp(F(x)^\top G(y)) \leq c_1$ with probability one, we have that for any $\delta > 0$ and $x \in \mathcal{X}$, with probability at least $1 - \delta$, the following holds for all $F \in \mathcal{F}$ and $G \in \mathcal{G}$:

$$\mathbb{E}_{\bar{y}}[\exp(F(x)^\top G(y))] - \frac{1}{B} \sum_{k=1}^B \exp(F(x)^\top G(\hat{y}_k)) \leq 2 \sup_{x \in \mathcal{X}} \mathcal{R}_B(\mathcal{H}_{\mathcal{F},\mathcal{G},e}^x) + c_1 \sqrt{\frac{\ln(1/\delta)}{2B}}, \quad (12)$$

where

$$\sup_{x \in \mathcal{X}} \mathcal{R}_B(\mathcal{H}_{\mathcal{F},\mathcal{G},e}^x) = \sup_{x \in \mathcal{X}} \mathbb{E}_{y,\sigma} \left[\sup_{h_x \in \mathcal{H}_{\mathcal{F},\mathcal{G},e}^x} \frac{1}{B} \sum_{i=1}^B \sigma_i h_x(y_i) \right],$$

and

$$\mathcal{H}_{\mathcal{F},\mathcal{G},e}^x = \{y \mapsto \exp(F(x)^\top G(y)) : F \in \mathcal{F}, G \in \mathcal{G}\}.$$

Recall that $\gamma(x) = \mathbb{E}_{\bar{y}}[\exp(F(x)^\top G(y))] - \frac{1}{B} \sum_{k=1}^B \exp(F(x)^\top G(\hat{y}_k))$ is c_9 -Lipschitz; i.e., $|\gamma(x) - \gamma(x')| \leq c_9 \|x - x'\|_2$ for all $x \in \mathcal{X}$ where $\|x\|_2 \leq c_8$ for all $x \in \mathcal{X}$. For any metric space (\mathcal{M}, d) and subset $M \subseteq \mathcal{M}$, the (closed) ball of radius r at centered at c is denoted by $\mathcal{B}_{(\mathcal{M},d)}[c, r] = \{x \in \mathcal{M} : d(x, c) \leq r\}$, and the r -converging number of M with the covering \mathcal{C} is defined by

$$\mathcal{N}_{\mathcal{C}}(r, M) = \min \{|\mathcal{C}| : \mathcal{C} \subseteq \mathcal{M}, M \subseteq \cup_{c \in \mathcal{C}} \mathcal{B}_{(\mathcal{M},d)}[c, r]\}.$$

Let us choose the metric space (\mathcal{M}, d) to be the Euclidian space \mathbb{R}^κ with the Euclidian metric. That is, we have the ϵ -covering of \mathcal{X} with the Euclidean balls of radius r , with the r -converging number of

$$\mathcal{N}_{\mathcal{C}}(r, \mathcal{X}) \leq (2c_8\sqrt{\kappa}/r)^\kappa.$$

Thus, by setting $r = \frac{2c_8}{\sqrt{B}}$,

$$\mathcal{N}_{\mathcal{C}}(r, \mathcal{X}) \leq (\sqrt{\kappa B})^\kappa.$$

Using these,

$$\begin{aligned} \sup_{x \in \mathcal{X}} \gamma(x) &= \inf_{c \in \mathcal{C}} \sup_{x \in \mathcal{X}} \gamma(x) - \gamma(c) + \gamma(c) \leq \inf_{c \in \mathcal{C}} \sup_{x \in \mathcal{X}} |\gamma(x) - \gamma(c)| + \sup_{c \in \mathcal{C}} \gamma(c) \\ &\leq rc_9 + \sup_{c \in \mathcal{C}} \gamma(c) \\ &= \frac{2c_8c_9}{\sqrt{B}} + \sup_{c \in \mathcal{C}} \gamma(c). \end{aligned}$$

Here, using equation 12 with union bounds, we have that for any $\delta > 0$, with probability at least $1 - \delta$, the following holds for all $F \in \mathcal{F}$ and $G \in \mathcal{G}$:

$$\sup_{c \in \mathcal{C}} \gamma(c) \leq 2 \sup_{x \in \mathcal{X}} \mathcal{R}_B(\mathcal{H}_{\mathcal{F}, \mathcal{G}, e}^x) + c_1 \sqrt{\frac{\ln(\sqrt{\kappa B})^\kappa / \delta}{2B}} \leq 2 \sup_{x \in \mathcal{X}} \mathcal{R}_B(\mathcal{H}_{\mathcal{F}, \mathcal{G}, e}^x) + c_1 \sqrt{\frac{\kappa \ln(\sqrt{\kappa B} / \delta)}{2B}}.$$

Therefore, for any $\delta > 0$, with probability at least $1 - \delta$, the following holds for all $F \in \mathcal{F}$ and $G \in \mathcal{G}$:

$$\begin{aligned} \sup_{x \in \mathcal{X}} \gamma(x) &\leq 2 \sup_{x \in \mathcal{X}} \mathcal{R}_B(\mathcal{H}_{\mathcal{F}, \mathcal{G}, e}^x) + \frac{2c_8}{\sqrt{B}} + c_1 \sqrt{\frac{\kappa \ln(\sqrt{\kappa B} / \delta)}{2B}} \\ &= 2 \sup_{x \in \mathcal{X}} \mathcal{R}_B(\mathcal{H}_{\mathcal{F}, \mathcal{G}, e}^x) + \frac{1}{\sqrt{2B}} \left(2\sqrt{2}c_8c_9 + c_1 \sqrt{\kappa \ln(\sqrt{\kappa B} / \delta)} \right). \end{aligned} \quad (13)$$

Combining equations equation 11 and equation 13 with union bound, we have that for any $\delta > 0$, with probability at least $1 - \delta$,

$$\bar{\ell}_M(x, y) - \hat{\ell}_B(x, y) \quad (14)$$

$$= \frac{\exp(F(x)^\top G(y)) \left(\mathbb{E}_{\bar{y}}[\exp(F(x)^\top G(y))] - \frac{1}{B} \sum_{k=1}^B \exp(F(x)^\top G(\hat{y}_k)) \right)}{\left(\frac{1}{B} \sum_{k=1}^B \exp(F(x)^\top G(\hat{y}_k)) \right) \mathbb{E}_{\bar{y}}[\exp(F(x)^\top G(\bar{y}))]} \quad (15)$$

$$\leq \frac{\exp(F(x)^\top G(y)) \left(\frac{1}{\sqrt{2B}} \left(2\sqrt{2}c_8 + c_1 \sqrt{\kappa \ln(c_9\sqrt{\kappa B} / \delta)} \right) + 2 \sup_{x \in \mathcal{X}} \mathcal{R}_B(\mathcal{H}_{\mathcal{F}, \mathcal{G}, e}^x) \right)}{\left(\frac{1}{B} \sum_{k=1}^B \exp(F(x)^\top G(\hat{y}_k)) \right) \mathbb{E}_{\bar{y}}[\exp(F(x)^\top G(\bar{y}))]} \quad (16)$$

By defining

$$A(x, y) = \frac{\exp(F(x)^\top G(y))}{\left(\frac{1}{B} \sum_{k=1}^B \exp(F(x)^\top G(\hat{y}_k)) \right) \mathbb{E}_{\bar{y}}[\exp(F(x)^\top G(\bar{y}))]},$$

we have that for any $\delta > 0$, with probability at least $1 - \delta$,

$$\begin{aligned} & \mathbb{E}_{x,y}[\bar{\ell}_M(x,y) - \hat{\ell}_B(x,y)] \\ & \leq c_1 \mathbb{E}_{x,y}[A(x,y)] \left(\frac{1}{\sqrt{2B}} \left(2\sqrt{2}c_8c_9 + c_1 \sqrt{\kappa \ln(\sqrt{\kappa B}/\delta)} \right) + \frac{2}{c_1} \sup_{x \in \mathcal{X}} \mathcal{R}_B(\mathcal{H}_{\mathcal{F},\mathcal{G},e}^x) \right). \end{aligned} \quad (17)$$

For the second term, using Lemma 4 with the assumption that $\hat{\ell}_B(x,y) \leq c_2$ for $(x,y) \sim p_{(x,y)}$, we have that for any $\delta > 0$, with probability at least $1 - \delta$, the following holds for all $F \in \mathcal{F}$ and $G \in \mathcal{G}$:

$$\mathbb{E}_{x,y}[\hat{\ell}_B(x,y)] - \hat{\mathbb{E}}_S[\hat{\ell}_B(x,y)] \quad (18)$$

$$= \mathbb{E}_{x,y}[\hat{\ell}_B(x,y)] - \frac{1}{m} \sum_{i=1}^m \frac{B \exp(F(\hat{x}_i)^\top G(\hat{y}_i))}{\sum_{k=1}^B \exp(F(\hat{x}_i)^\top G(\hat{y}_k))} \leq 2\mathcal{R}_m(\mathcal{H}_{\mathcal{F},\mathcal{G},\hat{\ell}_B}) + c_2 \sqrt{\frac{\ln(1/\delta)}{2m}}, \quad (19)$$

where $\mathcal{H}_{\mathcal{F},\mathcal{G},\hat{\ell}_B} = \{(x,y) \mapsto \hat{\ell}_B(x,y) : F \in \mathcal{F}, G \in \mathcal{G}\}$. Combining equation 7, equation 17, and equation 18 with union bound, we have that for any $\delta > 0$, with probability at least $1 - \delta$, the following holds all $F \in \mathcal{F}$ and $G \in \mathcal{G}$:

$$\begin{aligned} & \mathbb{E}_{x,y}[\bar{\ell}_M(x,y)] - \hat{\mathbb{E}}_S[\hat{\ell}_B(x,y)] \\ & \leq c_1 \mathbb{E}_{x,y}[A(x,y)] \left(\frac{1}{\sqrt{2B}} \left(2\sqrt{2}c_8c_9 + c_1 \sqrt{\kappa \ln(\sqrt{\kappa B}/\delta)} \right) + \frac{2}{c_1} \sup_{x \in \mathcal{X}} \mathcal{R}_B(\mathcal{H}_{\mathcal{F},\mathcal{G},e}^x) \right) \\ & \quad + 2\mathcal{R}_m(\mathcal{H}_{\mathcal{F},\mathcal{G},\hat{\ell}_B}) + c_2 \sqrt{\frac{\ln(2/\delta)}{2m}}. \end{aligned}$$

■

The proof of Lemma 3 partially builds up on Lemma 4 below. Lemma 4 is a direct application of previous results (Bartlett and Mendelson, 2002; Mohri et al., 2012; Shalev-Shwartz and Ben-David, 2014) to our problem. We provide a proof of Lemma 4 by slightly modifying the proof of a previous work (Mohri et al., 2012, Theorem 3.1) for the completeness (the proof utilizes the nonnegativity of h to have a slightly tighter bound than Theorem 26.5 of Shalev-Shwartz and Ben-David, 2014):

Lemma 4 *Let \mathcal{H} be a set of maps $z \mapsto h(z)$ such that $h(z) \in [0, \lambda]$ for all z in its domain. Then, for any $\delta > 0$, with probability at least $1 - \delta$ over an i.i.d. draw of m i.i.d. samples $(z_i)_{i=1}^m$, the following holds for all maps $h \in \mathcal{H}$:*

$$\mathbb{E}_z[h(z)] \leq \frac{1}{m} \sum_{i=1}^m h(z_i) + 2\mathcal{R}_m(\mathcal{H}) + \lambda \sqrt{\frac{\ln(1/\delta)}{2m}}, \quad (20)$$

where $\mathcal{R}_m(\mathcal{H}) := \mathbb{E}_{(z_1, \dots, z_m), \sigma} [\sup_{h \in \mathcal{H}} \frac{1}{m} \sum_{i=1}^m \sigma_i h(z_i)]$ where $\sigma_1, \dots, \sigma_m$ are independent uniform random variables taking values in $\{-1, 1\}$.

Proof Let $S = (z_i)_{i=1}^m$ and $S' = (z'_i)_{i=1}^m$. Define

$$\varphi(S) = \sup_{h \in \mathcal{H}} \mathbb{E}_{x,y}[h(z)] - \frac{1}{m} \sum_{i=1}^m h(z_i). \quad (21)$$

To apply McDiarmid's inequality to $\varphi(S)$, we compute an upper bound on $|\varphi(S) - \varphi(S')|$ where S and S' be two test datasets differing by exactly one point of an arbitrary index i_0 ; i.e., $S_i = S'_i$ for all $i \neq i_0$ and $S_{i_0} \neq S'_{i_0}$. Then,

$$\varphi(S') - \varphi(S) \leq \sup_{h \in \mathcal{H}} \frac{h(z_{i_0}) - h(z'_{i_0})}{m} \leq \frac{\lambda}{m}. \quad (22)$$

Thus, by McDiarmid's inequality, for any $\delta > 0$, with probability at least $1 - \delta$,

$$\varphi(S) \leq \mathbb{E}_S[\varphi(S)] + \lambda \sqrt{\frac{\ln(1/\delta)}{2m}}. \quad (23)$$

Moreover,

$$\mathbb{E}_S[\varphi(S)] \quad (24)$$

$$= \mathbb{E}_S \left[\sup_{h \in \mathcal{H}} \mathbb{E}_{S'} \left[\frac{1}{m} \sum_{i=1}^m h(z'_i) \right] - \frac{1}{m} \sum_{i=1}^m h(z_i) \right] \quad (25)$$

$$\leq \mathbb{E}_{S, S'} \left[\sup_{h \in \mathcal{H}} \frac{1}{m} \sum_{i=1}^m (h(z'_i) - h(z_i)) \right] \quad (26)$$

$$\leq \mathbb{E}_{\xi, S, S'} \left[\sup_{h \in \mathcal{H}} \frac{1}{m} \sum_{i=1}^m \xi_i (h(z'_i) - h(z_i)) \right] \quad (27)$$

$$\leq 2\mathbb{E}_{\xi, S} \left[\sup_{h \in \mathcal{H}} \frac{1}{m} \sum_{i=1}^m \xi_i h(z_i) \right] = 2\mathcal{R}_m(\mathcal{H}) \quad (28)$$

where the first line follows the definitions of each term, the second line uses the Jensen's inequality and the convexity of the supremum, and the third line follows that for each $\xi_i \in \{-1, +1\}$, the distribution of each term $\xi_i(h(z'_i) - h(z_i))$ is the distribution of $(h(z'_i) - h(z_i))$ since S and S' are drawn iid with the same distribution. The fourth line uses the subadditivity of supremum. ■

H.1.1 ANALYZING $\sup_{x \in \mathcal{X}} \mathcal{R}_B(\mathcal{H}_{\mathcal{F}, \mathcal{G}, e}^x)$ AND $\mathcal{R}_m(\mathcal{H}_{\mathcal{F}, \mathcal{G}, \hat{\ell}_B})$

The bound in Lemma 3 contains two complex terms, $\sup_{x \in \mathcal{X}} \mathcal{R}_B(\mathcal{H}_{\mathcal{F}, \mathcal{G}, e}^x)$ and $\mathcal{R}_m(\mathcal{H}_{\mathcal{F}, \mathcal{G}, \hat{\ell}_B})$, that are challenging to interpret and to be further analyzed. The following two lemmas bound those two terms by more interpretable quantities:

Lemma 5 *Let \mathcal{F} be a set of maps $x \mapsto F(x)$ and \mathcal{G} be a set of maps $y \mapsto G(y)$. Then,*

$$\sup_{x \in \mathcal{X}} \mathcal{R}_B(\mathcal{H}_{\mathcal{F}, \mathcal{G}, e}^x) \leq c_1 c_3 \mathbb{E}_{y, \sigma} \left[\sup_{G \in \mathcal{G}} \frac{1}{B} \left\| \sum_{i=1}^B \sigma_i G(y_i) \right\|_2 \right].$$

Proof Since the derivative of exponential function $\exp(q)$ is $\exp(q)$ and we assume $\exp(F(x)^\top G(y)) \leq c_1$, the exponential function in the bounded domain of $\exp(F(x)^\top G(y)) \leq c_1$ has Lipschitz constant of c_1 .

Therefore,

$$\begin{aligned}
\mathbb{E}_{y,\sigma} \left[\sup_{h_x \in \mathcal{H}_{\mathcal{F},\mathcal{G},e}^x} \frac{1}{B} \sum_{i=1}^B \sigma_i h_x(y_i) \right] &= \mathbb{E}_{y,\sigma} \left[\sup_{F \in \mathcal{F}, G \in \mathcal{G}} \frac{1}{B} \sum_{i=1}^B \sigma_i \exp(F(x)^\top G(y_i)) \right] \\
&\leq c_1 \mathbb{E}_{y,\sigma} \left[\sup_{F \in \mathcal{F}, G \in \mathcal{G}} \frac{1}{B} \sum_{i=1}^B \sigma_i F(x)^\top G(y_i) \right] \\
&= \frac{c_1}{B} \mathbb{E}_{y,\sigma} \left[\sup_{F \in \mathcal{F}, G \in \mathcal{G}} F(x)^\top \sum_{i=1}^B \sigma_i G(y_i) \right]. \\
&\leq \frac{c_1}{B} \mathbb{E}_{y,\sigma} \left[\sup_{F \in \mathcal{F}, G \in \mathcal{G}} \|F(x)\|_2 \left\| \sum_{i=1}^B \sigma_i G(y_i) \right\|_2 \right] \\
&\leq \frac{c_1}{B} \left(\sup_{F \in \mathcal{F}} \|F(x)\|_2 \right) \mathbb{E}_{y,\sigma} \left[\sup_{G \in \mathcal{G}} \left\| \sum_{i=1}^B \sigma_i G(y_i) \right\|_2 \right] \\
&= c_1 \left(\sup_{F \in \mathcal{F}} \|F(x)\|_2 \right) \mathbb{E}_{y,\sigma} \left[\sup_{G \in \mathcal{G}} \frac{1}{B} \left\| \sum_{i=1}^B \sigma_i G(y_i) \right\|_2 \right].
\end{aligned}$$

Therefore,

$$\begin{aligned}
\sup_{x \in \mathcal{X}} \mathcal{R}_B(\mathcal{H}_{\mathcal{F},\mathcal{G},e}^x) &= \sup_{x \in \mathcal{X}} \mathbb{E}_{y,\sigma} \left[\sup_{h_x \in \mathcal{H}_{\mathcal{F},\mathcal{G},e}^x} \frac{1}{B} \sum_{i=1}^B \sigma_i h_x(y_i) \right] \\
&\leq c_1 \left(\sup_{x \in \mathcal{X}, F \in \mathcal{F}} \|F(x)\|_2 \right) \mathbb{E}_{y,\sigma} \left[\sup_{G \in \mathcal{G}} \frac{1}{B} \left\| \sum_{i=1}^B \sigma_i G(y_i) \right\|_2 \right].
\end{aligned}$$

■

Lemma 6 Let \mathcal{F} be a set of maps $x \mapsto F(x)$ and \mathcal{G} be a set of maps $y \mapsto G(y)$. Then,

$$\mathcal{R}_m(\mathcal{H}_{\mathcal{F},\mathcal{G},\hat{\ell}_B}) \leq \sqrt{2}c_4 \sqrt{c_5^2 + c_6^2} \sum_{k=1}^D (\mathcal{R}_m(\mathcal{F}_k) + \mathcal{R}_m(\mathcal{G}_k)).$$

where $\mathcal{F}_k = \{x \mapsto F(x)_k : F \in \mathcal{F}\}$ and $\mathcal{G}_k = \{y \mapsto G(y)_k : G \in \mathcal{G}\}$.

Proof Recall that

$$\mathcal{H}_{\mathcal{F},\mathcal{G},\hat{\ell}_B} = \{(x, y) \mapsto \hat{\ell}_B(x, y) : F \in \mathcal{F}, G \in \mathcal{G}\}$$

Using the definitions,

$$\begin{aligned}
\mathcal{R}_m(\mathcal{H}_{\mathcal{F},\mathcal{G},\hat{\ell}_B}) &= \mathbb{E}_{(x,y),\sigma} \left[\sup_{h \in \mathcal{H}_{\mathcal{F},\mathcal{G},\hat{\ell}_B}} \frac{1}{m} \sum_{i=1}^m \sigma_i h(x_i, y_i) \right] \\
&= \mathbb{E}_{(x,y),\sigma} \left[\sup_{F \in \mathcal{F}, G \in \mathcal{G}} \frac{1}{m} \sum_{i=1}^m \sigma_i \hat{\ell}_B(x_i, y_i) \right] \\
&= \frac{1}{m} \mathbb{E}_{(x,y),\sigma} \left[\sup_{F \in \mathcal{F}, G \in \mathcal{G}} \sum_{i=1}^m \sigma_i \frac{B \exp(F(x_i)^\top G(y_i))}{\sum_{k=1}^B \exp(F(x_i)^\top G(\hat{y}_k))} \right].
\end{aligned}$$

Define

$$h(p, q) = \frac{B \exp(p^\top q)}{\sum_{k=1}^B \exp(p^\top G(\hat{y}_k))}.$$

Then,

$$\mathcal{R}_m(\mathcal{H}_{\mathcal{F},\mathcal{G},\hat{\ell}_B}) = \frac{1}{m} \mathbb{E}_{(x,y),\sigma} \left[\sup_{F \in \mathcal{F}, G \in \mathcal{G}} \sum_{i=1}^m \sigma_i h(F(x_i), G(y_i)) \right].$$

Moreover,

$$\frac{\partial h(p, q)}{\partial p} = \frac{B \exp(p^\top q)}{\sum_{k=1}^B \exp(p^\top G(\hat{y}_k))} q^\top - \frac{B \exp(p^\top q)}{\left(\sum_{k=1}^B \exp(p^\top G(\hat{y}_k)) \right)^2} \left(\sum_{k=1}^B \exp(p^\top G(\hat{y}_k)) G(\hat{y}_k)^\top \right)$$

$$\frac{\partial h(p, q)}{\partial q} = \frac{B \exp(p^\top q)}{\sum_{k=1}^B \exp(p^\top G(\hat{y}_k))} p^\top.$$

Therefore,

$$\begin{aligned}
\|\nabla h(p, q)\|_2^2 &= \left(\frac{\exp(p^\top q)}{\frac{1}{B} \sum_{k=1}^B \exp(p^\top G(\hat{y}_k))} \right)^2 \left[\sum_{i=1}^D \left(q_i - \frac{\sum_{k=1}^B \exp(p^\top G(\hat{y}_k)) G(\hat{y}_k)_i}{\sum_{k=1}^B \exp(p^\top G(\hat{y}_k))} \right)^2 + \sum_{i=1}^D p_i^2 \right] \\
&\leq c_4^2 (c_5^2 + c_6^2).
\end{aligned}$$

Thus,

$$\|\nabla h(p, q)\|_2 \leq c_4 \sqrt{c_5^2 + c_6^2}.$$

Using a vector-contraction inequality, i.e., Corollary 4 of (Maurer, 2016) with the additional expectation of both sides of the inequality, we have that

$$\begin{aligned}
& \mathcal{R}_m(\mathcal{H}_{\mathcal{F},\mathcal{G},\hat{\ell}_B}) \\
&= \frac{1}{m} \mathbb{E}_{(x,y),\sigma} \left[\sup_{F \in \mathcal{F}, G \in \mathcal{G}} \sum_{i=1}^m \sigma_i h(F(x_i), G(y_i)) \right] \\
&\leq \frac{\sqrt{2}c_4 \sqrt{c_5^2 + c_6^2}}{m} \mathbb{E}_{(x,y),\sigma} \left[\sup_{F \in \mathcal{F}, G \in \mathcal{G}} \sum_{i=1}^m \sum_{k=1}^D \sigma_{ik} F(x_i)_k + \sum_{i=1}^m \sum_{j=1}^D \sigma_{ij} G(y_i)_j \right] \\
&\leq \frac{\sqrt{2}c_4 \sqrt{c_5^2 + c_6^2}}{m} \mathbb{E}_{(x,y),\sigma} \left[\sup_{F \in \mathcal{F}} \sum_{i=1}^m \sum_{k=1}^D \sigma_{ik} F(x_i)_k + \sup_{G \in \mathcal{G}} \sum_{i=1}^m \sum_{j=1}^D \sigma_{ij} G(y_i)_j \right] \\
&= \frac{\sqrt{2}c_4 \sqrt{c_5^2 + c_6^2}}{m} \left(\mathbb{E}_{(x,y),\sigma} \left[\sup_{F \in \mathcal{F}} \sum_{i=1}^m \sum_{k=1}^D \sigma_{ik} F(x_i)_k \right] + \mathbb{E}_{(x,y),\sigma} \left[\sup_{G \in \mathcal{G}} \sum_{i=1}^m \sum_{j=1}^D \sigma_{ij} G(y_i)_j \right] \right) \\
&\leq \frac{\sqrt{2}c_4 \sqrt{c_5^2 + c_6^2}}{m} \left(\sum_{k=1}^D \mathbb{E}_{x,\sigma} \left[\sup_{f \in \mathcal{F}_k} \sum_{i=1}^m \sigma_i f(x_i) \right] + \sum_{k=1}^D \mathbb{E}_{y,\sigma} \left[\sup_{g \in \mathcal{G}_k} \sum_{i=1}^m \sigma_i g(y_i) \right] \right) \\
&= \sqrt{2}c_4 \sqrt{c_5^2 + c_6^2} \left(\sum_{k=1}^D \mathcal{R}_m(\mathcal{F}_k) + \sum_{k=1}^D \mathcal{R}_m(\mathcal{G}_k) \right)
\end{aligned}$$

■

H.1.2 COMBINING ALL TOGETHER FOR THE GENERAL CASE

We now combine the above lemmas to complete the proof of Theorem 2:

Proof [Proof of Theorem 2] From Lemma 3, we have that for any for any $\delta > 0$, with probability at least $1 - \delta$, the following holds for all $F \in \mathcal{F}$ and $G \in \mathcal{G}$:

$$\begin{aligned}
& \mathbb{E}_{x,y}[\bar{\ell}_M(x,y)] - \hat{\mathbb{E}}_S[\hat{\ell}_B(x,y)] \\
&\leq c_1 \mathbb{E}_{x,y}[A(x,y)] \left(\frac{1}{\sqrt{2B}} \left(2\sqrt{2}c_8c_9 + c_1 \sqrt{\kappa \ln(\sqrt{\kappa B}/\delta)} \right) + \frac{2}{c_1} \sup_{x \in \mathcal{X}} \mathcal{R}_B(\mathcal{H}_{\mathcal{F},\mathcal{G},e}^x) \right) \\
&\quad + 2\mathcal{R}_m(\mathcal{H}_{\mathcal{F},\mathcal{G},\hat{\ell}_B}) + c_2 \sqrt{\frac{\ln(2/\delta)}{2m}}.
\end{aligned}$$

Then by using Lemma 5 and 6,

$$\begin{aligned}
& \mathbb{E}_{x,y}[\bar{\ell}_M(x,y)] - \hat{\mathbb{E}}_S[\hat{\ell}_B(x,y)] \\
& \leq c_1 \mathbb{E}_{x,y}[A(x,y)] \left(\frac{1}{\sqrt{2B}} \left(2\sqrt{2}c_8c_9 + c_1 \sqrt{\kappa \ln(\sqrt{\kappa B}/\delta)} \right) + 2c_3 \mathbb{E}_{y,\sigma} \left[\sup_{G \in \mathcal{G}} \frac{1}{B} \left\| \sum_{i=1}^B \sigma_i G(y_i) \right\|_2 \right] \right) \\
& \quad + 2\sqrt{2}c_4 \sqrt{c_5^2 + c_6^2} \sum_{k=1}^D (\mathcal{R}_m(\mathcal{F}_k) + \mathcal{R}_m(\mathcal{G}_k)) + c_2 \sqrt{\frac{\ln(2/\delta)}{2m}} \\
& = \frac{C_1}{\sqrt{2B}} + C_2 \mathcal{R}_B(G) + C_3 \sum_{k=1}^D (\mathcal{R}_m(\mathcal{F}_k) + \mathcal{R}_m(\mathcal{G}_k)) + c_2 \sqrt{\frac{\ln(2/\delta)}{2m}}.
\end{aligned}$$

■

H.2 Bounding $\mathbb{E}_{y,\sigma} \left[\sup_{G \in \mathcal{G}} \frac{1}{B} \left\| \sum_{i=1}^B \sigma_i G(y_i) \right\|_2 \right]$ and $\sum_{k=1}^D (\mathcal{R}_m(\mathcal{F}_k) + \mathcal{R}_m(\mathcal{G}_k))$ for the special case with deep neural networks

We now want to bound $\mathbb{E}_{y,\sigma} \left[\sup_{G \in \mathcal{G}} \left\| \sum_{i=1}^m \sigma_i G(y_i) \right\|_2 \right]$ and $\sum_{k=1}^D (\mathcal{R}_m(\mathcal{F}_k) + \mathcal{R}_m(\mathcal{G}_k))$ in the case where F and G represent deep neural networks. We consider standard deep neural networks, of the form

$$G(y) = (\omega_L \circ \sigma_{L-1} \circ \omega_{L-1} \circ \sigma_{L-2} \cdots \sigma_1 \circ \omega_1)(y)$$

$$F(x) = (\omega'_{L'} \circ \sigma'_{L'-1} \circ \omega'_{L'-1} \circ \sigma'_{L'-2} \cdots \sigma'_1 \circ \omega'_1)(x)$$

where $\omega_l(q) = W_l q$ and σ_l is an element-wise activation function. Similarly, $\omega'_l(q) = W'_l q$ and σ'_l is an element-wise activation function.

Lemma 7 *Suppose that the function σ_l is 1-Lipschitz and positive homogeneous for all $l \in [L-1]$ and $\|y\|_2 \leq c_7$ for all $y \in \mathcal{Y}$. Let $\mathcal{G} = \{y \mapsto G(y) : (\forall l \in [L]) [\|W_l\|_F \leq M_l]\}$. Then,*

$$\mathbb{E}_{y,\sigma} \left[\sup_{G \in \mathcal{G}} \frac{1}{B} \left\| \sum_{i=1}^B \sigma_i G(y_i) \right\|_2 \right] \leq \frac{c_7(\sqrt{2 \log(2)}L + 1)(\prod_{l=1}^L M_l)}{\sqrt{B}}.$$

Proof Since

$$\begin{aligned}
\left\| \sum_{i=1}^B \sigma_i G(y_i) \right\|_2 &= \left\| \sum_{i=1}^B \sigma_i W_L (\sigma_{L-1} \circ \omega_{L-1} \circ \sigma_{L-2} \cdots \sigma_1 \circ \omega_1)(y) \right\|_2 \\
&\leq \|W_L\|_F \left\| \sum_{i=1}^B \sigma_i (\sigma_{L-1} \circ \omega_{L-1} \circ \sigma_{L-2} \cdots \sigma_1 \circ \omega_1)(y) \right\|_2,
\end{aligned}$$

the proof steps of Theorem 1 of (Golowich et al., 2018) work to bound $\mathbb{E}_\sigma \left[\sup_{G \in \mathcal{G}} \left\| \sum_{i=1}^B \sigma_i G(y_i) \right\|_2 \right]$. Therefore, using the proof of Theorem 1 of (Golowich et al., 2018),

$$\mathbb{E}_\sigma \left[\sup_{G \in \mathcal{G}} \frac{1}{B} \left\| \sum_{i=1}^B \sigma_i G(y_i) \right\|_2 \right] \leq \frac{c_7(\sqrt{2 \log(2)}L + 1)(\prod_{l=1}^L M_l)}{\sqrt{B}}$$

Lemma 8 Suppose that the function σ'_l is 1-Lipschitz and positive homogeneous for all $l \in [L-1]$ and $\|x\| \leq c_8$ for all $x \in \mathcal{X}$. Let $\mathcal{F} = \{x \mapsto F(x) : (\forall l \in [L'-1])[\|W'_l\|_F \leq M'_l] \wedge \|(W'_l)_k\|_F \leq M'_{L',k}\}$ where $(W'_l)_k$ is the k -th row of W'_l . Suppose that the function σ_l is 1-Lipschitz and positive homogeneous for all $l \in [L-1]$ and $\|y\| \leq c_7$ for all $y \in \mathcal{Y}$. Let $\mathcal{G} = \{y \mapsto G(y) : (\forall l \in [L-1])[\|W_l\|_F \leq M_l] \wedge \|(W_L)_k\|_F \leq M_{L,k}\}$ where $(W_l)_k$ is the k -th row of W_l . Then,

$$\begin{aligned} & \sum_{k=1}^D (\mathcal{R}_m(\mathcal{F}_k) + \mathcal{R}_m(\mathcal{G}_k)) \\ & \leq \frac{c_7(\sqrt{2\log(2)L} + 1)(\prod_{l=1}^{L-1} M_l) \sum_{k=1}^D M_{L,k}}{\sqrt{m}} + \frac{c_8(\sqrt{2\log(2)L'} + 1)(\prod_{l=1}^{L'-1} M'_l) \sum_{k=1}^D M'_{L',k}}{\sqrt{m}} \end{aligned}$$

and

$$\mathbb{E}_{y,\sigma} \left[\sup_{G \in \mathcal{G}} \frac{1}{B} \left\| \sum_{i=1}^B \sigma_i G(y_i) \right\|_2 \right] \leq \frac{c_7(\sqrt{2\log(2)L} + 1)(\prod_{l=1}^{L-1} M_l) \sqrt{\sum_{k=1}^D M_{L,k}^2}}{\sqrt{B}}.$$

Proof From Theorem 1 of (Golowich et al., 2018), we have that

$$\mathcal{R}_m(\mathcal{F}_k) \leq \frac{c_8(\sqrt{2\log(2)L'} + 1)(\prod_{l=1}^{L'-1} M'_l) M'_{L',k}}{\sqrt{m}}$$

and

$$\mathcal{R}_m(\mathcal{G}_k) \leq \frac{c_7(\sqrt{2\log(2)L} + 1)(\prod_{l=1}^{L-1} M_l) M_{L,k}}{\sqrt{m}}.$$

Thus,

$$\begin{aligned} & \sum_{k=1}^D (\mathcal{R}_m(\mathcal{F}_k) + \mathcal{R}_m(\mathcal{G}_k)) \\ & \leq \sum_{k=1}^D \left(\frac{c_7(\sqrt{2\log(2)L} + 1)(\prod_{l=1}^{L-1} M_l) M_{L,k}}{\sqrt{m}} + \frac{c_8(\sqrt{2\log(2)L'} + 1)(\prod_{l=1}^{L'-1} M'_l) M'_{L',k}}{\sqrt{m}} \right). \end{aligned}$$

This proves the first statement. For the second statement, since $\|(W_l)_k\|_F \leq M_{L,k}$, we have that

$$\|W_L\|_F^2 = \sum_{k=1}^D \|(W_L)_k\|_F^2 \leq \sum_{k=1}^D M_{L,k}^2.$$

This implies that $\|W_l\|_F \leq \sqrt{\sum_{k=1}^D M_{L,k}^2}$. Thus, using Lemma 7,

$$\mathbb{E}_{y,\sigma} \left[\sup_{G \in \mathcal{G}} \frac{1}{B} \left\| \sum_{i=1}^B \sigma_i G(y_i) \right\|_2 \right] \leq \frac{c_7(\sqrt{2\log(2)L} + 1)(\prod_{l=1}^{L-1} M_l) \sqrt{\sum_{k=1}^D M_{L,k}^2}}{\sqrt{B}}.$$

H.3 Combining all together for the special case with deep neural networks

We now combine the above lemmas to complete the proof of Theorem 1 for the special case with deep neural networks:

Proof [Proof of Theorem 1] From Lemma 3, for any \mathcal{F} and \mathcal{G} , and for any $\delta > 0$, with probability at least $1 - \delta$, the following holds for all $F \in \mathcal{F}$ and $G \in \mathcal{G}$:

$$\begin{aligned} & \mathbb{E}_{x,y}[\bar{\ell}_M(x,y)] - \hat{\mathbb{E}}_S[\hat{\ell}_B(x,y)] \\ & \leq c_1 \mathbb{E}_{x,y}[A(x,y)] \left(\frac{1}{\sqrt{2B}} \left(2\sqrt{2}c_8c_9 + c_1\sqrt{\kappa \ln(\sqrt{\kappa B}/\delta)} \right) + \frac{2}{c_1} \sup_{x \in \mathcal{X}} \mathcal{R}_B(\mathcal{H}_{\mathcal{F},\mathcal{G},e}^x) \right) \\ & \quad + 2\mathcal{R}_m(\mathcal{H}_{\mathcal{F},\mathcal{G},\hat{\ell}_B}) + c_2\sqrt{\frac{\ln(2/\delta)}{2m}}, \end{aligned}$$

where Lemma 5 and Lemma 6 show that

$$\sup_{x \in \mathcal{X}} \mathcal{R}_B(\mathcal{H}_{\mathcal{F},\mathcal{G},e}^x) \leq c_1c_3\mathbb{E}_{y,\sigma} \left[\sup_{G \in \mathcal{G}} \frac{1}{B} \left\| \sum_{i=1}^B \sigma_i G(y_i) \right\|_2 \right],$$

and

$$\mathcal{R}_m(\mathcal{H}_{\mathcal{F},\mathcal{G},\hat{\ell}_B}) \leq \sqrt{2}c_4\sqrt{c_5^2 + c_6^2} \sum_{k=1}^D (\mathcal{R}_m(\mathcal{F}_k) + \mathcal{R}_m(\mathcal{G}_k)).$$

Finally, using Lemma 8 for the particular \mathcal{F} and \mathcal{G} with deep neural networks, we have that

$$\begin{aligned} & \sum_{k=1}^D (\mathcal{R}_m(\mathcal{F}_k) + \mathcal{R}_m(\mathcal{G}_k)) \\ & \leq \frac{c_7(\sqrt{2\log(2)L} + 1)(\prod_{l=1}^{L-1} M_l) \sum_{k=1}^D M_{L,k}}{\sqrt{m}} + \frac{c_8(\sqrt{2\log(2)L'} + 1)(\prod_{l=1}^{L'-1} M'_l) \sum_{k=1}^D M'_{L',k}}{\sqrt{m}} \end{aligned}$$

and

$$\mathbb{E}_{y,\sigma} \left[\sup_{G \in \mathcal{G}} \frac{1}{B} \left\| \sum_{i=1}^B \sigma_i G(y_i) \right\|_2 \right] \leq \frac{c_7(\sqrt{2\log(2)L} + 1)(\prod_{l=1}^{L-1} M_l) \sqrt{\sum_{k=1}^D M_{L,k}^2}}{\sqrt{B}}.$$

Combining those, we have that for any $\delta > 0$, with probability at least $1 - \delta$, the following holds for all $F \in \mathcal{F}$ and $G \in \mathcal{G}$:

$$\begin{aligned}
& \mathbb{E}_{x,y}[\bar{\ell}_M(x, y)] - \hat{\mathbb{E}}_S[\hat{\ell}_B(x, y)] \\
& \leq c_1 \mathbb{E}_{x,y}[A(x, y)] \left(\frac{1}{\sqrt{2B}} \left(2\sqrt{2}c_8c_9 + c_1\sqrt{\kappa \ln(\sqrt{\kappa B}/\delta)} \right) + 2c_3 \mathbb{E}_{y,\sigma} \left[\sup_{G \in \mathcal{G}} \frac{1}{B} \left\| \sum_{i=1}^B \sigma_i G(y_i) \right\|_2 \right] \right) \\
& \quad + 2\sqrt{2}c_4 \sqrt{c_5^2 + c_6^2} \sum_{k=1}^D (\mathcal{R}_m(\mathcal{F}_k) + \mathcal{R}_m(\mathcal{G}_k)) + c_2 \sqrt{\frac{\ln(2/\delta)}{2m}} \\
& \leq c_1 \mathbb{E}_{x,y}[A(x, y)] \frac{1}{\sqrt{2B}} \left(2\sqrt{2}c_8c_9 + c_1\sqrt{\kappa \ln(\sqrt{\kappa B}/\delta)} \right) \\
& \quad + c_1 \mathbb{E}_{x,y}[A(x, y)] 2\sqrt{2}c_3 \frac{c_7(\sqrt{2 \log(2)L} + 1)(\prod_{l=1}^{L-1} M_l) \sqrt{\sum_{k=1}^D M_{L,k}^2}}{\sqrt{2B}} \\
& \quad + 2\sqrt{2}c_4 \sqrt{c_5^2 + c_6^2} \frac{c_7(\sqrt{2 \log(2)L} + 1)(\prod_{l=1}^{L-1} M_l) \sum_{k=1}^D M_{L,k}}{\sqrt{m}} \\
& \quad + 2\sqrt{2}c_4 \sqrt{c_5^2 + c_6^2} \frac{c_8(\sqrt{2 \log(2)L'} + 1)(\prod_{l=1}^{L'-1} M'_l) \sum_{k=1}^D M'_{L',k}}{\sqrt{m}} \\
& \quad + c_2 \sqrt{\frac{\ln(2/\delta)}{2m}} \\
& \leq \frac{Q_1}{\sqrt{m}} + \frac{Q_2}{\sqrt{2B}} + c_2 \sqrt{\frac{\ln(2/\delta)}{2m}}
\end{aligned}$$

■